Linköping University | Department of Electrical Engineering
Master's thesis, 30 ECTS | Division of Vehicular Systems
2023 | LiTH-ISY-EX--23/5593--SE

Thermal Modelling of Permanent Magnet Synchronous Motor Windings in Heavy-Duty Electric Vehicles

Ken Dahl

Supervisor : Max Johansson
Examiner : Erik Frisk

External supervisor : Iman Shafikhani, Scania CV AB

Linköpings universitet
SE–581 83 Linköping
+46 13 28 10 00 , www.liu.se

Abstract

A significant challenge with permanent magnet synchronous motors (PMSMs) is thermal management. Thermal stress can lead to irreversible damage to components, and to enable efficient cooling, a thermal model is needed. In this thesis paper, methods for estimating the hot spot temperature of the windings in PMSMs used in heavy-duty EVs are investigated. The methods include black-box models and lumped parameter thermal network-based models. The results reveal that the implemented models are not sufficient for achieving the desired accuracy, and indicate that more parts of the windings need to be considered.

Acknowledgments

Firstly, I would like to thank Vaheed Nezhadali for giving me the opportunity to conduct my master's thesis at Scania. Thank you, everyone at NECC, for welcoming me with open arms.

Special thanks to Iman Shafikhani and Max Johansson. Your input has been invaluable. Without your help, this project would take ages.

Thank you, Erik Frisk, for your guidance throughout the project.

Finally, thank you, Matilda, for everything you do for me. You mean the world to me.

Contents

1 Introduction

A key factor in the struggle against climate change is the electrification of the automotive industry [1]. The main component of electric vehicle (EV) propulsion is electric machines (EMs), and a type of EM that is gaining in popularity is the permanent magnet synchronous motor (PMSM) [2]. Figures 1.1 and 1.2 depict an EM and the cross-section of a PMSM, highlighting its different components. Part of the PMSM's success is due to its power density and torque density [3], leading to efficiency at low speeds and causing it to replace the typical induction motor. However, as the production of PMSMs is draining our planet of rare-earth permanent magnets [4] and as high temperatures can cause damage to its components [5], the importance of operating PMSMs in a sustainable manner grows.

In heavy-duty EVs such as electric trucks, the same trend can be observed as for passenger car EVs [6]. Though, as the trucks weigh more, they pose greater constraints on their motors in terms of thermal management. In order to cool PMSMs appropriately, knowledge of their temperature is extremely relevant.

In this master's thesis, different thermal models for PMSM windings were investigated for the purpose of simplifying thermal management. In the midst of global warming, this might lengthen the life of heavy-duty EV motors and, consequently, contribute positively to the environment.

1.1 Motivation

As a PMSM runs, power losses in different components lead to heat development. Thermal stress can cause degradation in winding insulation, permanent magnets, and bearings [5], while the maximum temperature of a PMSM is limited by the winding insulation or permanent magnets [8]. During heavy workloads, it is possible for the windings to reach over 180 °C, while the temperature limit of the windings is 155 °C or less for several insulation classes [9]. To prevent temperatures from rising too high, liquid cooling and torque limiting are common. However, in order to know when to cool the motor and limit the torque, awareness of the PMSM's maximum temperature (a.k.a. hot spot temperature) is necessary. Measuring the temperature of the different parts of the EM is not always feasible, though. The temperature gradient is not uniform in every component, meaning that multiple sensors are

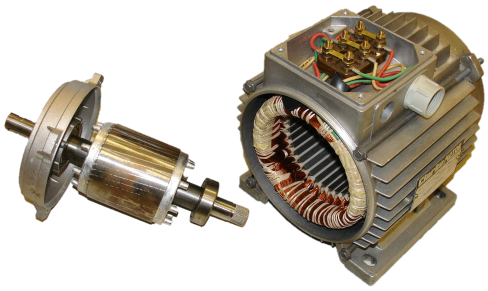

Figure 1.1: The rotor (left) and stator (right) of an electric machine [7]. Licensed under a Creative Commons Attribution-ShareAlike 3.0 Unported License.

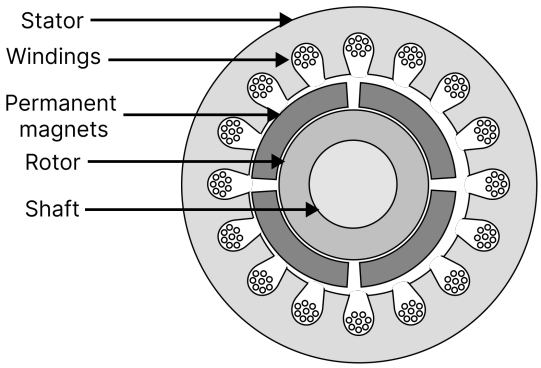

Figure 1.2: The cross-section of a PMSM.

required to cover the whole machine to measure the hot spot temperature accurately. These sensors can be expensive as well as difficult to install and maintain and are therefore rarely beneficial to use. Thus, an accurate model is necessary.

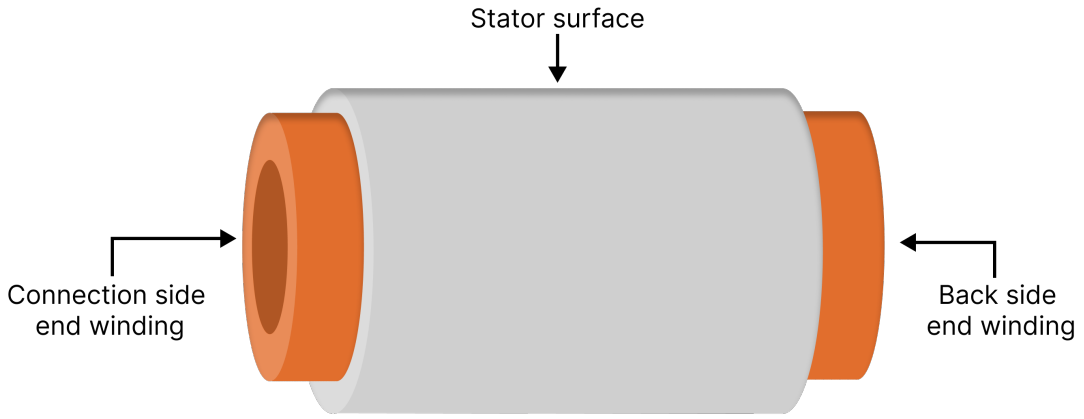

Figure 1.3: A sketch of a PMSM stator and its windings, without the rotor and permanent magnets. The orange regions represent the end windings while the grey region represents the stator surface.

1.2 Aim

This thesis aimed to investigate different methods for modelling the hot spot temperature of PMSM windings. This included the connection side end windings, the back side end winding, and the winding running through the stator (in this thesis called the mid-stack winding). These are pointed out in Figure 1.3. Accuracy goals were set for all temperatures, where overestimation was limited to 5 °C and underestimation to 2.5 °C. The reason for the goals being more ambitious for underestimation than for overestimation was due to the importance of not exceeding certain temperatures.

1.3 Research questions

The thesis attempted to answer the following questions:

- How do common black-box models for estimating the hot spot temperature of PMSM windings perform?
- How can physical knowledge of a PMSM be incorporated in the construction of a model that fulfils the desired accuracy?

1.4 Delimitations

The thesis project was time-limited to 20 weeks including planning, implementation, and report writing. A limited number of sensors for measuring the temperature of the windings were used in producing the available experimental data. The sensors were positioned closely together in three groups; at the connection side end windings, back side end windings, and the mid-stack windings. Note that the winding temperature sensors were installed on test rigs and not in the PMSMs used in trucks, hence the need for the model. Dimensions for the PMSM and physical attributes of the coolant were not considered. The real-time computational speeds of the models were not evaluated as the models were assumed to be lightweight enough to run on the hardware, even when considering hardware limitations and coexistence with the concurrently running software. Furthermore, different methods for neither normalising data nor initialising the produced models were investigated in this thesis.

2 Theory and related works

This chapter presents relevant theory and related works for the modelling of PMSMs and dynamic systems in general.

2.1 Dynamic system modelling

Approaches for modelling dynamic systems can be split into four different categories: data-driven, analytical, numerical, and hybrid [10]. Data-driven models, or black-box models, are derived solely from experimental data. A type of data-driven modelling is parametric modelling, where a general model design is chosen, whereby its parameters are estimated. In analytical approaches, equations based on physical formulas describe the system. Numerical approaches are used when solutions to the physical expressions do not exist and have to be approximated instead. A hybrid model implies that multiple approaches are combined.

2.2 Black-box model structures

While systems generally are non-linear in practice, linear methods can occasionally model the dynamics of the system. This section describes widely used linear and non-linear models for parametric system identification.

Linear models

A general model format for linear models is given in [11] as

$$A(q)y(t) = \frac{B(q)}{F(q)}u(t) + \frac{C(q)}{D(q)}e(t), \tag{2.1}$$

where,

$$A(q) = 1 + a_1 q^{-1} + ... + a_{n_a} q^{-n_a}, \tag{2.2}$$

$$B(q) = q^{-n_k}(b_0 + b_1 q^{-1} + ... + b_{n_b} q^{-n_b}), \tag{2.3}$$

$$C(q) = 1 + c_1 q^{-1} + ... + c_{n_c} q^{-n_c}, \tag{2.4}$$

$$D(q) = 1 + d_1 q^{-1} + ... + d_{n_d} q^{-n_d}, \tag{2.5}$$

$$F(q) = 1 + f_1 q^{-1} + ... + f_{n_f} q^{-n_f}, \tag{2.6}$$

and $y(t), u(t)$ and $e(t)$ are output, input and measurement noise, respectively. Furthermore, q is the time shift operator while n_a, n_b, n_c, n_d, n_f and n_k are integer design parameters specifying the order of the polynomials $A(q), B(q), C(q), D(q)$ and $F(q)$. By letting some of them be equal to 1, some common models can be obtained.

With $A(q) = 1$, the Box-Jenkins model is obtained. It allows for modelling the measurement noise without any dependence on the dynamics of the system.

With $C(q) = D(q) = F(q) = 1$, we get the ARX (Auto-Regressive with eXogenous inputs) model. It is often used for system identification since predictors are automatically stable while it easily can be estimated using simple techniques such as the linear least squares method [12]. Measurement errors can, however, not always be characterised which may lead to inconsistent models.

The ARMAX (Auto-Regressive Moving-Average with eXogenous inputs) model is attained with $D(q) = F(q) = 1$. For its predictors to be stable, only $C(q)$ has to be stable, and unlike the ARX model, the ARMAX model can model measurement errors.

The OE (Output-Error) model is obtained with $A(q) = C(q) = D(q) = 1$, meaning that measurement noise can not be modelled. This is useful if the dynamics of the system alone are to be modelled.

Non-linear models

In [13], a general polynomial form of the NARX (Non-linear ARX) model is given in discrete time by

$$y_i = F^{(n_p)}(y_{i-1}, ..., y_{i-n_y}; x_{i-1}, ...x_{i-n_x}), \tag{2.7}$$

where n_p is the maximum model order. Additionally, y_i and x_i are the input and output, respectively, at time step i. According to [13], any system can be represented by (2.7) given a model order of sufficient degree.

The NARX model does, however, assume that the measurement data does not contain any noise which can complicate the modelling process. To address this, the NARMAX (Non-linear Auto-Regressive Moving-Average with eXogenous inputs) model considers noisy measurements and can be described as

$$y_i = F^{(n_p)}(y_{i-1}, ..., y_{i-n_y}; x_{i-1}, ...x_{i-n_x}; e_{i-1}, ...e_{i-n_e}) + e_i, \tag{2.8}$$

where e_i is white noise.

In [14], parameters of a MIMO (Multi-Input Multi-Output) system are identified using a Hammerstein-Wiener (HW) model. While considering white measurement noise and coloured process noise, the problem was solved using a Maximum Likelihood Expectation Maximisation algorithm.

2.3 Model order selection

Selecting the order of a model is about finding a balance between bias and variance [15]. The more parameters used in a model, i.e., the larger the model order, the less biased the model is. However, as the number of parameters increases, the variance grows. Additionally, with an increased model order, computational demands for calculating and using the model grow.

One way to estimate the order of a system is by analysing the matrix

$$R^s(N) = \frac{1}{N}\sum_{t=1}^{N} \varphi_s(t)\varphi_s^T(t), \tag{2.9}$$

where $\varphi_s(t) = [-y(t-1)... - y(t-s)\ u(t-1)...u(t-s)]^T$ and N is the number of samples. It will be non-singular for $s \leqslant n$ and singular for $s \geqslant n+1$ where n is the true order. For MIMO (Multi-Input Multi-Output) systems, this is done for every input-output pair.

2.4 Model validation

After estimating a model of a system, the next step is to evaluate the performance of the model on new data the model has not seen before. Aside from the simulated output of the model fitting nicely to the validation data, there are several indications that a model has captured the dynamics of the system. Comparing Bode plots of parametric models to the estimated frequency functions of the system is one way. Another validation method is to reduce the order of the model. If this can be done without the behaviour of the model being affected, the initial model was unnecessarily large. Moreover, the standard deviation of the estimated parameters could give an indication that the model is too large. The parameter should perhaps be removed if the confidence interval includes zero. [15]

The normalised root mean square error (NRMSE) can be used to quantify the similarity of two signals. In system modelling, it can thus evaluate how well the output of a model fits the measured data. A percentage between 100% and $-\infty$%, where 100% means that the signals are the same, can be calculated by:

$$100(1 - \text{NRMSE}) = 100\left(1 - \frac{\sqrt{\sum_{t=1}^{N}(y(t) - \hat{y}(t))^2}}{\sqrt{\sum_{t=1}^{N}(y(t) - \hat{\bar{y}}(t))^2}}\right)\ [16]. \tag{2.10}$$

Here, y is the measured data, $\hat{y}$ is the model output, and $\hat{\bar{y}}$ is the mean value of $\hat{y}$.

Residual analysis

The residuals of a model are the difference between the measured and estimated values and can give hints on whether a model has captured the dynamics of the system [15]. For instance, correlation between the residuals and previous inputs indicates that the model can be enhanced. The same can be concluded if correlation is found among the residuals themselves.

2.5 Heat transfer theory

There exist three essential modes of heat transfer; conduction, convection, and radiation [17]. Conduction is when heat, by virtue of the temperature gradient in a body, flows through a solid or through a fluid at rest [18]. Convection is when heat is transferred between a flowing fluid and a body [19]. Radiation is when energy is emitted from a body by means of its moving atoms [20], allowing heat transfer between bodies without the need for a medium between them.

Fluid flow in a pipe

The Reynolds number, Re, describes if the flow of a fluid in a pipe is laminar (smooth) or turbulent [21]. It is defined as:

$$\mathrm{Re} = \frac{d\dot{V}\rho}{\mu}, \tag{2.11}$$

where d is the internal diameter of the pipe, $\dot{V}$ is the flow speed, while ρ and μ are the density and dynamic viscosity of the fluid.

The Prandtl number, Pr, is the ratio between a fluid's capability to transfer momentum and its capability to transfer energy and is defined as:

$$\mathrm{Pr} = \frac{\mu c}{k} \quad [21]. \tag{2.12}$$

Here, c is the specific heat capacity of the fluid, and k is its thermal conductivity.

The Nusselt number, Nu, describing the ratio between convective and conductive heat transfer is defined in [22] as:

$$\mathrm{Nu} = \frac{h}{k/d} = \frac{hd}{k}, \tag{2.13}$$

where h is the heat transfer coefficient of the flow. In [23], a correlation for the Nusselt number, specifically for laminar flow, is provided using the length of the pipe, L:

$$\mathrm{Nu} = 3.66 + \frac{0.065\ \mathrm{Re}\ \mathrm{Pr}\ \frac{d}{L}}{1 + 0.04(\mathrm{Re}\ \mathrm{Pr}\ \frac{d}{L})^{\frac{2}{3}}}. \tag{2.14}$$

With knowledge of pipe dimensions, flow speed, and fluid properties, (2.11) – (2.14) can be combined to find h.

Specific heat capacity of copper and iron

The temperature dependence of the specific heat capacities of copper and iron can be seen in Table 2.1.

Table 2.1: Specific heat capacities in J K^{-1} mol^{-1} of copper (Cu) and iron (Fe) at different temperatures in K and a constant pressure of 0.1 MPa [24].

T	100	200	300	400	500	600	700	800
C_{Cu}	16.010	22.631	24.462	25.318	25.912	26.481	26.996	27.494
C_{Fe}	12.101	21.588	25.140	27.386	29.702	32.049	34.602	37.949

Dynamic system expression

To derive a dynamic heat transfer expression for a system of bodies, Newton's law of external heat transfer can first be used to describe the heat flow, G, between a body and its surroundings:

$$G = h(T - T_0) \quad [25]. \tag{2.15}$$

Here, h is the heat transfer coefficient between body and surroundings, T is the temperature of the body, and T_0 is the temperatures of the surroundings. The heat flow can also be described using the surface area of the heat transfer, A, and the change in thermal energy, Q, by:

$$G = -\frac{1}{A}\frac{\partial Q}{\partial t}. \tag{2.16}$$

The basic formula of calorimetry, in turn, describes the change in Q in terms of change in temperature:

$$dQ = c\,m\,dT = C\,dT, \tag{2.17}$$

where c, m, and C are the specific heat capacity, mass, and heat capacity of the body. A combination of (2.15) - (2.17) might be written as:

$$C\frac{dT(t)}{dt} = hA(T_0(t) - T(t)), \tag{2.18}$$

describing the change of temperature in a body as a first-order differential equation. By considering power losses, P, in the material of the body adding heat, (2.18) becomes:

$$C\frac{dT(t)}{dt} = hA(T_0(t) - T(t)) + P(t). \tag{2.19}$$

Finally, for a body, i, in contact with multiple neighbours, j, such as other bodies or fluids, (2.19) can be extended into:

$$C_i\frac{dT_i(t)}{dt} = \sum_j h_{ij}A_{ij}(T_j(t) - T_i(t)) + P_i(t). \tag{2.20}$$

2.6 Power losses in PMSMs

Two different types of power losses are generally considered in a PMSM; electric and magnetic losses [26]. The electrical losses occur in the copper windings and are computed by:

$$P = 3I^2R, \tag{2.21}$$

where I and R are the current and resistance of the windings. With a known resistance, R_0, at winding temperature T_0, the temperature dependency of the resistance can be described as:

$$R(T) = R_0(1 + \alpha(T - T_0)), \tag{2.22}$$

where α is the thermal coefficient of the material [26, 27]. If the power loss at temperature T_0 is known, the power loss at temperature T can then be calculated by:

$$P(T) = 3I^2R(T) = 3\frac{P(T_0)}{3R_0}R(T) = P(T_0)\frac{R(T)}{R_0}$$

$$= P(T_0)\frac{R_0(1 + \alpha(T - T_0))}{R_0} = P(T_0)(1 + \alpha(T - T_0)). \tag{2.23}$$

Magnetic power losses in the iron too, change with temperature [26]. These will, however, be assumed to have no temperature-dependency in this thesis.

2.7 Related works

In this section, some known methods for thermal modelling of PMSMs are described. Most papers in the area concern regular-sized EVs, while a few touch on other applications such as agricultural vehicles and railways.

Finite element method

By dividing a system into small subdomains, the finite element method (FEM) numerically solves partial differential equations describing the heat transfer between the domains [28]. Although it is known for producing accurate results, it is a computationally demanding method and is therefore not always feasible to use.

An example of PMSM thermal modelling using FEM can be seen in [29]. An agricultural EV with an air-cooled IPMSM (Interior PMSM) is studied, where the temperature of the winding is estimated. Electromagnetic field analysis was used for estimating the losses, while conduction, convection, and radiation were considered for the temperature modelling. The estimated winding temperature deviated from the experimentally acquired data by a maximum of 5° C, where the maximum temperature reached by the machine was just above 100° C.

Lumped parameter thermal network

A popular method for modelling the temperature in PMSMs is by using lumped parameter thermal networks (LPTNs) [28]. Like in FEM, LPTNs divide the system into smaller parts and estimate the temperature based on heat transfer relations. However, in LPTNs, subdomains (or lumps/nodes) are generally many times larger and can consist of whole components. Furthermore, an LPTN assumes that no temperature gradient exists in the nodes. Because of this, the method outputs the average temperatures of each node [30], making it quicker but less accurate than FEM.

Using a two-node LPTN, [8] models the temperature of the stator windings and permanent magnets of a water-cooled IPMSM. The results are promising as they only differ from experimentally obtained data by a maximum of $6^\circ C$. However, the model requires the stator core temperature to be measured and estimates the average temperatures instead of the hot spot temperatures. Without access to the stator core temperature measurement, a three-node LPTN can be derived as long as the properties of the coolant are known. Though, according to the paper, this approach would be less robust than the proposed two-node model. The paper claims that the presented model can be used in EVs as well as in heavier applications such as trains.

In [31], the temperature of an air-cooled IPMSM designed for EVs is first modelled with a three-node LPTN and then controlled using an MPC (Model Predictive Control) based strategy. The model estimates temperatures of the winding, end winding and rotor of the machine and is expressed in state-space form. Ambient and coolant temperatures, as well as losses in the components to be estimated, are assumed to be known or calculable. Although the results are accurate, the validation data is neither displayed in detail nor does it seem to be particularly varying.

An analytical model based on motor dimensions, thermal conductivity and other parameters is described in [30]. By complementing an average temperature estimating LPTN, it produces similar results to the computationally heavy FEM, all in a much shorter time. This is done by modelling the system in cartesian coordinates instead of the typically used cylindrical coordinates, avoiding complex computations.

Artificial neural network

A type of artificial neural network is the feed-forward neural network (FNN) where data is only sent forward in the information chain [32]. An FNN-based NARX black-box model for temperature estimation in PMSMs is proposed in [33]. Measurements from sensors on the

windings and permanent magnet are used in the training of the model, where temperatures range between 20° C and 130° C. The current, voltage, speed, and temperature of the coolant were used as inputs, producing an error of no more than 4.5° C on data with high fluctuations.

Using an LPTN-FNN hybrid model, the temperature of a water-cooled PMSM for car application is presented in [34]. The LPTN models the permanent magnet, stator tooth, stator winding and stator yoke, and its structure is used as a base model. Meanwhile, the FNN tunes the parameters of the LPTN which are related to losses and thermal conductances. The maximum temperature reached in the experiments was around 110° C and the maximum error was 5.5° C.

3 Methodology

This chapter covers the implementation and validation of the thermal models. Different black-box models were produced using *Matlab R2020b* with the help of functions from *System Identification Toolbox*. A lumped parameter thermal network (LPTN) was derived and implemented in both *Matlab* and *Simulink*. Parameters of the LPTN were calibrated using the *Parameter Estimator* app from the *Simulink Design Optimization* add-on. Lastly, model validation was performed in *Matlab*.

3.1 System discretisation

The windings of the PMSM were discretised into three nodes according to the temperature sensor placements; C (connection side end winding), M (mid-stack winding), and B (back side end winding). Figures 3.1-3.3 highlight the different parts of the PMSM that the nodes represent. The temperatures of the nodes were denoted T_C, T_M, and T_B.

Figure 3.1: The connection side end windings, denoted C.

Figure 3.2: The windings running through the stator were denoted M.

Figure 3.3: The back side end windings, denoted B.

3.2 Choice of data

Data from over 60 experiments were available, occupying approximately 9 GB of memory. These mainly included three types of driving modes; "step" experiments, where the torque resembled a step function and the temperatures rose steadily; "drive cycle" experiments, where the torque and temperature varied heavily; and "idle" experiments, where the torque was zero and the temperatures dropped steadily. Variations in the initial temperatures oc-

curred, making some step experiments differ largely in temperature rise. Examples of how the different types of experiments could look are depicted in Figure 3.4a, 3.4b, and 3.4c. Out of the available data, five step experiments and three drive cycle experiments containing high temperatures were chosen for this thesis. All experiments included 9 different signals that could be used as inputs to the models, as well as temperature measurements for nodes C, M, and B that could be used as outputs. Five experiments were used for the calibration of the models, where three were step experiments and two were drive cycles. For the validation of the models, three different experiments were used, where two were step experiments and one was a drive cycle experiment.

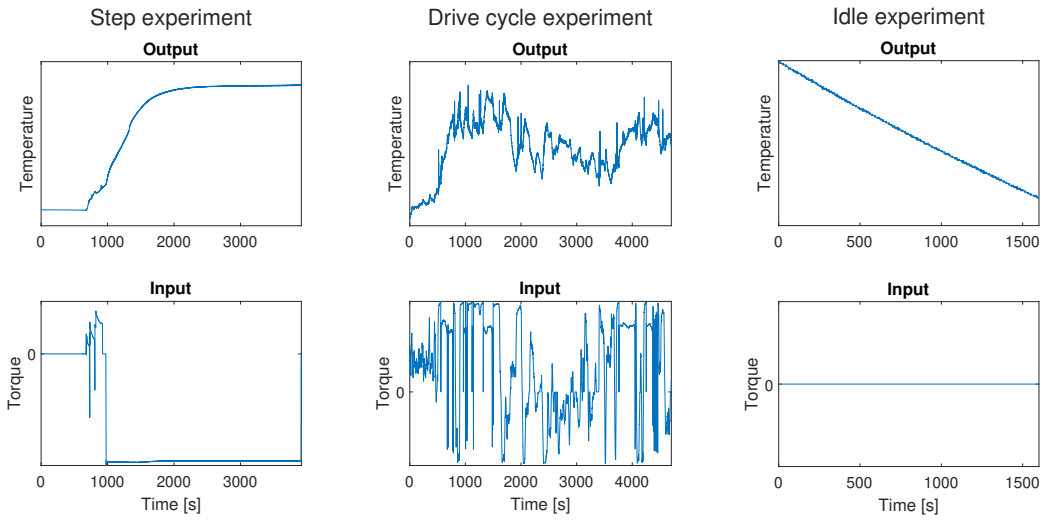

(a) Step experiment. (b) Drive cycle experiment. (c) Idle experiment.

Figure 3.4: Example data from the different experiment types. The input shown is the torque while the output is the hot spot temperature of node B.

3.3 Data pre-processing

Maximum and average temperatures of the nodes were extracted from the measurements. Since the temperature sensors for the mid-stack winding were positioned closely together at the stator midpoint, the average temperature calculations for M included the average temperatures of C and B as single sensor values.

To get rid of measurement noise and unrealistically quick-varying measurements in the calibration data, the signals were low-pass filtered. This was done using a Butterworth filter of order 5 at an appropriate cut-off frequency determined through trial and error.

3.4 Black-box modelling

The hot spot temperatures of C, M, and B were estimated using various black-box models mentioned in 2.2.

Normalisation

The calibration data for the black-box modelling were normalised to contain values between -0.5 and 0.5 by:

$$y_n = \frac{y - y_{\min}}{y_{\max} - y_{\min}} - 0.5, \tag{3.1}$$

where y was the signal to be normalised, y_{min} and y_{max} were the minimum and maximum values of the signal out of all calibration data, and y_n was the normalised signal. As the simulated model outputs were normalised, this was reversed by extracting y from (3.1):

$$y = (y_n + 0.5)(y_{\max} - y_{\min}) + y_{\min}. \tag{3.2}$$

Model order selection

To give a rough estimate of suitable model orders, (2.9) was analysed for the calibration data. This method suggested orders between 3 and 6, as seen in Table 3.1. During model calibration, different model orders for the different input-output pairs were, however, not used. Instead, one model order was chosen at a time and used for all input-output pairs. The time delay, n_k, was not estimated and was instead set to zero.

Table 3.1: Estimated model orders for each input-output pair, averaged over the 5 calibration experiments.

	u_1	u_2	u_3	u_4	u_5	u_6	u_7	u_8	u_9
y_1	4	3.2	4	5.6	5.4	3.4	3	3.2	5
y_2	4.8	4	5	5.6	5.6	4	4	4	5
y_3	4.6	4	4.6	5.8	5.8	4	4	4	6

Model structures

ARX, ARMAX, OE, BJ, NARX, and HW models were calibrated with the suggested model orders, as well as other orders. In an attempt to improve the estimation of T_M, the calibration was slightly modified so that the estimated values of T_C and T_B were used as additional inputs to the estimation of T_M.

3.5 Lumped parameter thermal network

An LPTN was developed for estimating the average temperatures in C, M, and B (see 3.6 for average to maximum temperature estimation). To facilitate the derivation of the equations, the stator and the coolant oil were discretised to form the nodes S (stator surface), OC (connection-side oil), OS (stator surface oil), and OB (back-side oil). Combined with the previously defined nodes, this resulted in a total of seven nodes as seen in Figure 3.5. The temperatures T_{OS} and T_{OB} were measured, while T_{OC} was assumed to be the average between T_{OS} and T_{OB}.

LPTN with 4 output nodes

Equation (2.20) was used to describe the temperature change in each of the output nodes; C, M, B, and S. The heat transfer coefficients and heat transfer surface areas were combined into a single parameter, $\lambda_{ij} = h_{ij}A_{ij}$. This, together with $\frac{dT_i(t)}{dt} = \dot{T}_i(t)$ yielded:

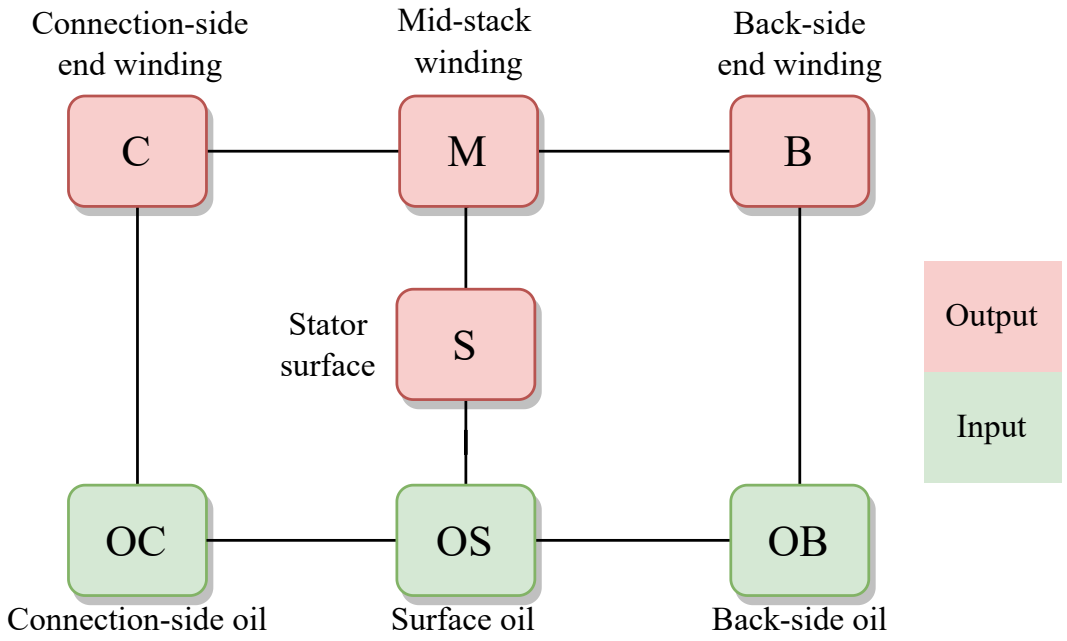

Figure 3.5: Overview of the thermal nodes of the LPTN. The lines represent heat transfer between nodes.

$$\dot{T}_C = \frac{\lambda_{MC}(T_M(t) - T_C(t)) + \lambda_{CO}(T_{OC}(t) - T_C(t)) + P_C(t)}{C_C}, \tag{3.3}$$

$$\dot{T}_M = \frac{\lambda_{MC}(T_C(t) - T_M(t)) + \lambda_{MB}(T_B(t) - T_M(t)) + \lambda_{MS}(T_S(t) - T_M(t)) + P_M(t)}{C_M}, \tag{3.4}$$

$$\dot{T}_B = \frac{\lambda_{MB}(T_M(t) - T_B(t)) + \lambda_{BO}(T_{OB}(t) - T_B(t)) + P_B(t)}{C_B}, \tag{3.5}$$

$$\dot{T}_S = \frac{\lambda_{MS}(T_M(t) - T_S(t)) + \lambda_{SO}(T_{OS}(t) - T_S(t)) + P_S(t)}{C_S}, \tag{3.6}$$

where λ_{Mk} and λ_{kO} were conductive and convective heat transfer coefficients, respectively for $k = \{C, B, S\}$.

LPTN with 3 output nodes

Since measurement data for the stator surface was not available, the stator surface equations were incorporated into the equation for the mid-stack winding. Differentiation of (3.4), assuming $\dot{C}_i = \dot{\lambda}_{ij} = 0 \; \forall i, j$, gave:

$$\ddot{T}_M(t) = \frac{\lambda_{MC}(\dot{T}_C(t) - \dot{T}_M(t)) + \lambda_{MB}(\dot{T}_B(t) - \dot{T}_M(t)) + \lambda_{MS}(\dot{T}_S(t) - \dot{T}_M(t)) + \dot{P}_M(t)}{C_M}, \tag{3.7}$$

where $\ddot{T}(t) = \frac{d^2T(t)}{dt^2}$. By rearranging (3.4), T_S could then be expressed as:

$$T_S(t) = \frac{C_M\dot{T}_M(t) - \lambda_{MC}(T_C(t) - T_M(t)) - \lambda_{MB}(T_B(t) - T_M(t)) - P_M(t)}{\lambda_{MS}} + T_M(t). \quad (3.8)$$

Inserting (3.8) in (3.6) and (3.6) in (3.7) allowed for expressing the mid-stack winding temperature without the need for the stator surface node:

$$\begin{aligned} C_M\ddot{T}_M(t) = {} & \dot{T}_M(-C_M\frac{\lambda_{MS}+\lambda_{SO}}{C_S} - \lambda_{MC} - \lambda_{MB}) + \dot{P}_M \\ & + T_C(\frac{\lambda_{MS}+\lambda_{SO}}{C_S} - \frac{\lambda_{MC}+\lambda_{CO}}{C_C})\lambda_{MC} \\ & + T_M(\frac{\lambda_{MC}^2}{C_C} + \frac{\lambda_{MB}^2}{C_B} - \frac{\lambda_{MC}\lambda_{MS} + \lambda_{MB}\lambda_{MS} + \lambda_{MC}\lambda_{SO} + \lambda_{MB}\lambda_{SO} + \lambda_{MS}\lambda_{SO}}{C_S}) \\ & + T_B(\frac{\lambda_{MS}+\lambda_{SO}}{C_S} - \frac{\lambda_{MB}+\lambda_{BO}}{C_B})\lambda_{MB} \\ & + T_{OC}\frac{\lambda_{MC}\lambda_{CO}}{C_C} + T_{OB}\frac{\lambda_{MB}\lambda_{BO}}{C_B} + T_{OS}\frac{\lambda_{MS}\lambda_{SO}}{C_S} \\ & + P_C\frac{\lambda_{MC}}{C_C} + P_M\frac{\lambda_{MS}+\lambda_{SO}}{C_S} + P_B\frac{\lambda_{MB}}{C_B} + P_S\frac{\lambda_{MS}}{C_S}. \end{aligned} \quad (3.9)$$

Power losses

Experimentally obtained values for the copper power losses at temperature T_0 were used in determining the temperature-dependent losses. They were calculated according to (2.23) as:

$$P_C = P_{Cu,EW}\ (1 + \alpha_{Cu}(T_C - T_0)), \quad (3.10)$$

$$P_M = P_{Cu,MW}\ (1 + \alpha_{Cu}(T_M - T_0)), \quad (3.11)$$

$$P_B = P_{Cu,EW}\ (1 + \alpha_{Cu}(T_B - T_0)). \quad (3.12)$$

Here, $P_{Cu,EW}$ and $P_{Cu,MW}$ were the electrical power losses in the end windings and the mid-stack winding. The power losses in S were simply:

$$P_S = P_{Fe}, \quad (3.13)$$

where P_{Fe} were experimentally obtained magnetic power losses in the iron at temperature T_0. These were, as mentioned in 2.6, assumed not dependent on temperature.

Heat capacities

The specific heat capacities for the copper windings and the iron stator were determined using Table 2.1 and linear interpolation. The values of the masses were optimised during the parameter calibration mentioned below. As T_S was not estimated, it was set to the average value of T_C, T_M, and T_B.

Temperature change to temperature

After calculating the temperature change of a node i, its temperature was then retrieved using the sample time, t_s, by:

$$T_i(t) = T_i(t-1) + t_s\dot{T}_i(t-1),$$

for the derivatives in (3.3) and (3.5), and

$$T_i(t) = T_i(t-1) + t_s\dot{T}_i(t-1) + \frac{1}{2}t_s^2\ddot{T}_i(t-1),$$

for the double derivative in (3.9).

Parameter calibration

The conductive parameters $\lambda_{MC}, \lambda_{MB}$, and λ_{MS}, as well as the masses, m_C, m_M, m_B and m_S, were calibrated as constant values. The convective parameters, $\lambda_{CO}, \lambda_{BO}$, and λ_{SO}, were, on the other hand, calibrated as third-order polynomials functions of the oil flow speed, $\dot{V}$:

$$\lambda_{iO} = k_{0,i} + k_{1,i}\dot{V} + k_{2,i}\dot{V}^2 + k_{3,i}\dot{V}^3,\ i = \{C, B, S\}. \tag{3.14}$$

3.6 LPTN to hot spot temperature

Two different methods for estimating the hot spot temperatures using the estimated average temperatures were implemented. In the first method, a simple relationship was expressed using the oil temperature of the PMSM, while the second involved black-box models.

Using an oil temperature-based model

In the measurement data, it was observed that a relationship existed between the temperature of the nodes and the temperature of the oil. As the oil temperature rose, the difference between the maximum and average winding temperatures, i.e. the temperature gradient, grew. An inactive PMSM, on the other hand, meant that the temperature gradient of the windings decreased, and their temperatures converged towards the oil temperature. The maximum temperatures were thus estimated by:

$$\begin{aligned} T_C^{max} &= T_C^{avg} + a_C(T_C^{avg} - T_{oil}^{avg}), \\ T_M^{max} &= T_M^{avg} + a_M(T_M^{avg} - T_{oil}^{avg}), \\ T_B^{max} &= T_B^{avg} + a_B(T_B^{avg} - T_{oil}^{avg}), \end{aligned} \tag{3.15}$$

where a_C, a_M, and a_B were constant calibration parameters.

Using black-box models

The difference between the windings' maximum and average temperatures was modelled using black-box methods. The calibration was done in the same way as in 3.4, using all available inputs including the ones already used in the LPTN. This produced a model henceforth called the MMA (Maximum Minus Average) model. An illustration of how the model calibration was implemented is shown in Figure 3.6.

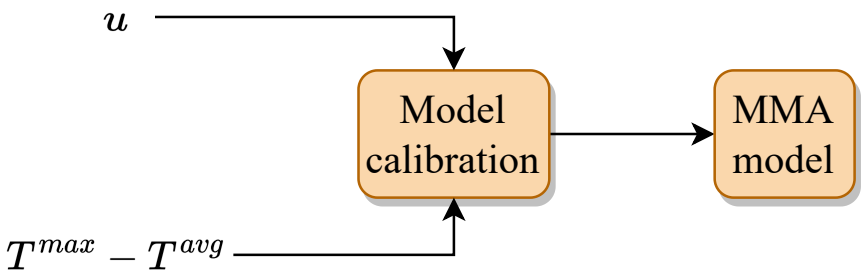

Figure 3.6: Calibration of the MMA (Maximum Minus Average) model, where u are the inputs and $T^{max} - T^{avg}$ are the outputs.

After the model calibration, the hot spot temperatures could be estimated by adding the estimated average temperature and the model output together, as seen in Figure 3.7.

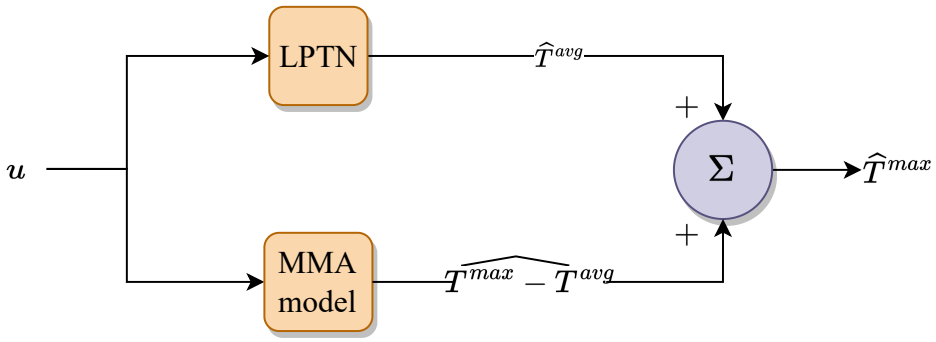

Figure 3.7: The hot spot estimation using the combined LPTN and black-box models.

3.7 Model validation

The model outputs were simulated with the validation experiment inputs, using the measured temperatures as initial values. The outputs were then validated through some of the methods mentioned in 2.4. Visual validation included comparing validation data and simulated outputs. Also, residuals were analysed by comparing them with the accuracy aims and observing their auto-correlation. To quantify the model performance, the model fits were calculated according to equation (2.10).

4 Results

This chapter is divided into three sections, each presenting the results from a separate validation experiment. For every method, figures that compare the simulated model outputs to the validation data, and that demonstrate how the models fare with the accuracy aims are shown. Figures indicating to which degree the models have captured the dynamics of the system are also displayed, along with tables of the model fit percentages.

The black-box models that were chosen to be presented were an ARX model of order 2, and NARX models of orders 1 and 2. These were in the figures denoted as *arx2*, *narx1*, and *narx2*. Modified black-box models, where T_C and T_B estimations were used as inputs for estimating T_M consisted of an ARX model of order 2 and a NARX model of order 1. These were denoted *arx2-mod* and *narx2-mod*. The LPTN was simply denoted *lptn*, while the oil temperature-based model was denoted *lptn-oil*. Finally, the LPTN-hybrid models were denoted *lptn-arx2* and *lptn-narx1*.

4.1 Validation experiment 1

The first validation experiment was a step experiment that began right after the temperatures had dropped from initially high values. Comparisons of measured and estimated temperatures and residual graphs are displayed below.

Output comparison

Figure 4.1 and 4.2 show temperature comparisons for the black-box models, Figure 4.3 and 4.4 for the modified black-box models, Figure 4.5 and 4.6 for the LPTN, Figure 4.7 and 4.8 for the LPTN and oil temperature combination, and lastly, Figure 4.9 and 4.10 for the LPTN-black-box models.

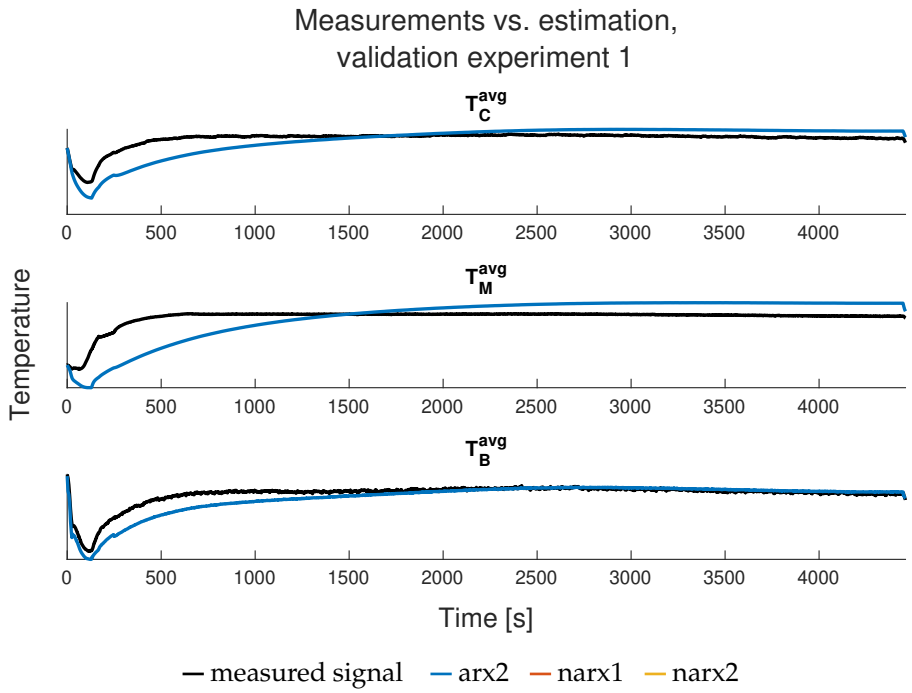

Figure 4.1: Comparison between validation experiment 1 and the simulated outputs of the black-box models.

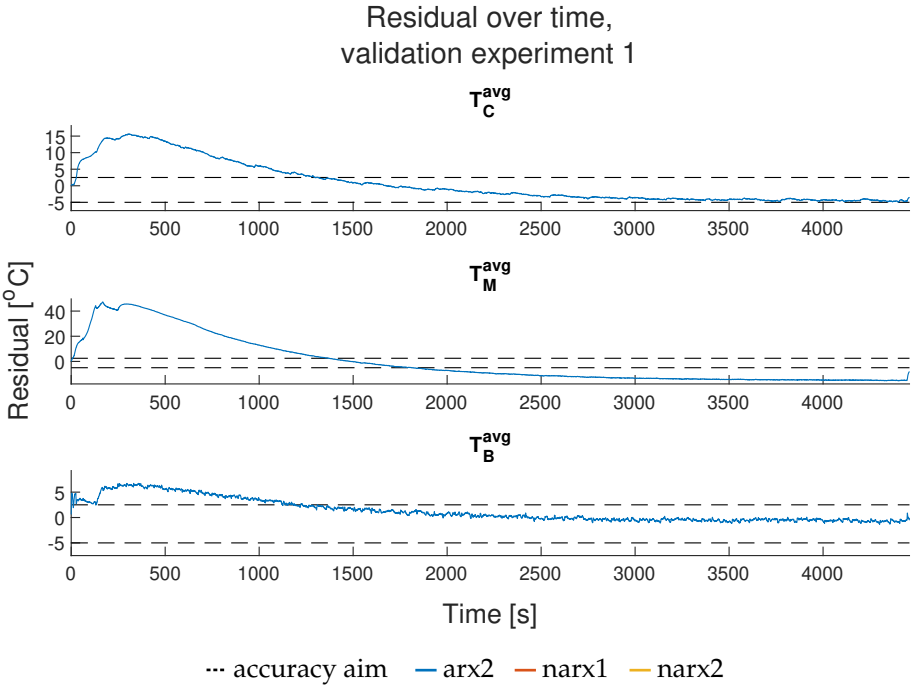

Figure 4.2: The residuals of the black-box models for validation experiment 1.

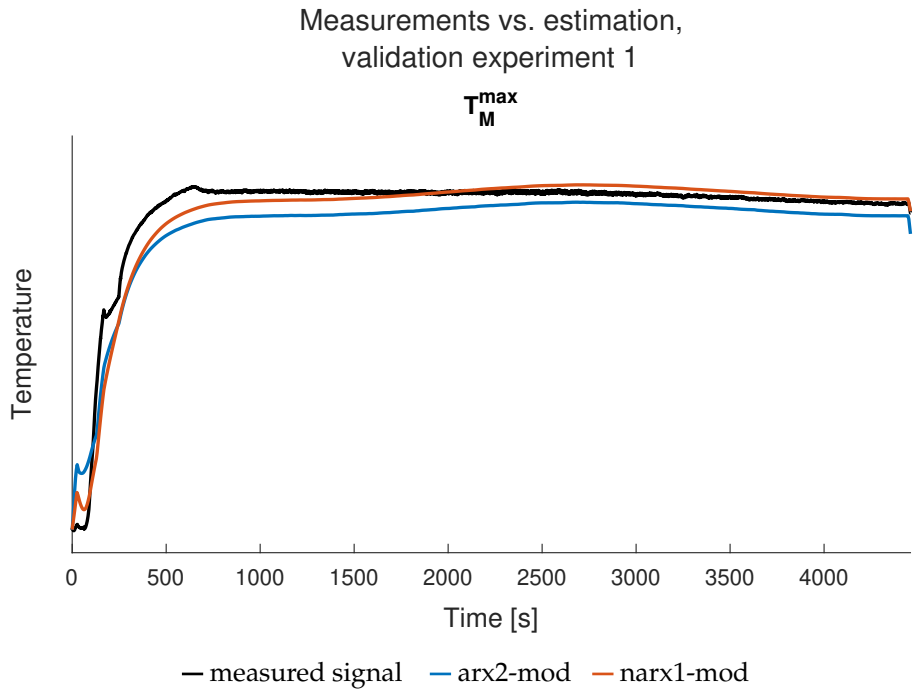

Figure 4.3: Comparison between validation experiment 1 and the simulated outputs of the modified black-box models.

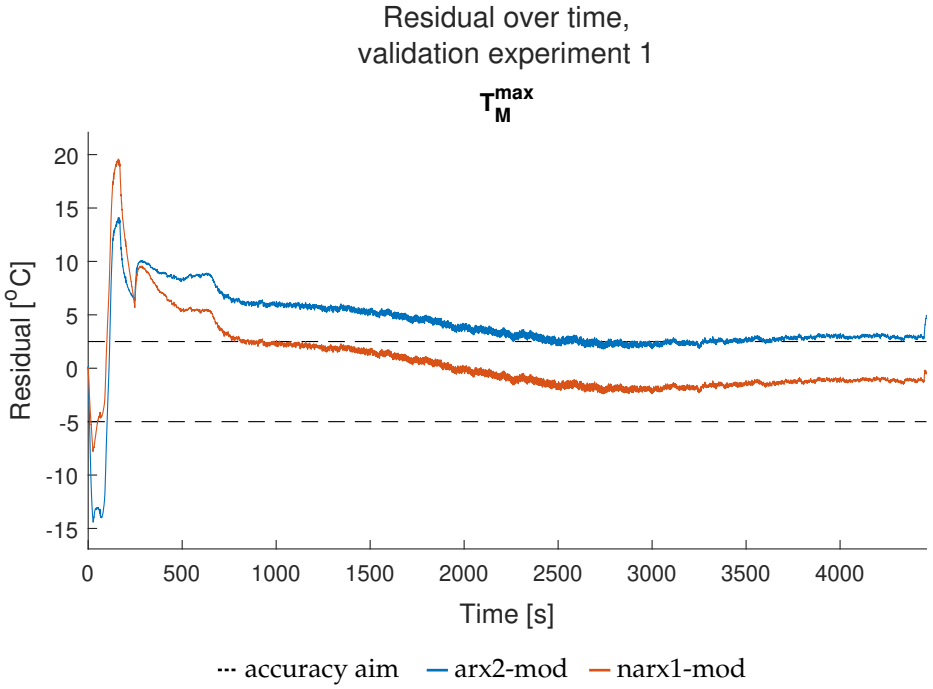

Figure 4.4: The residuals of the modified black-box models for validation experiment 1.

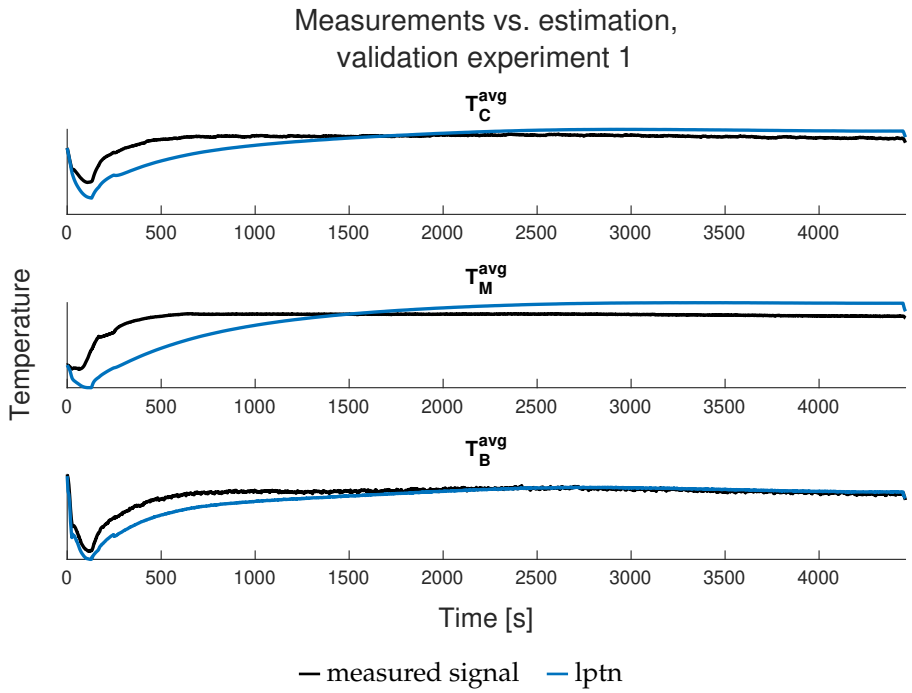

Figure 4.5: Comparison between validation experiment 1 and the simulated outputs of the LPTN.

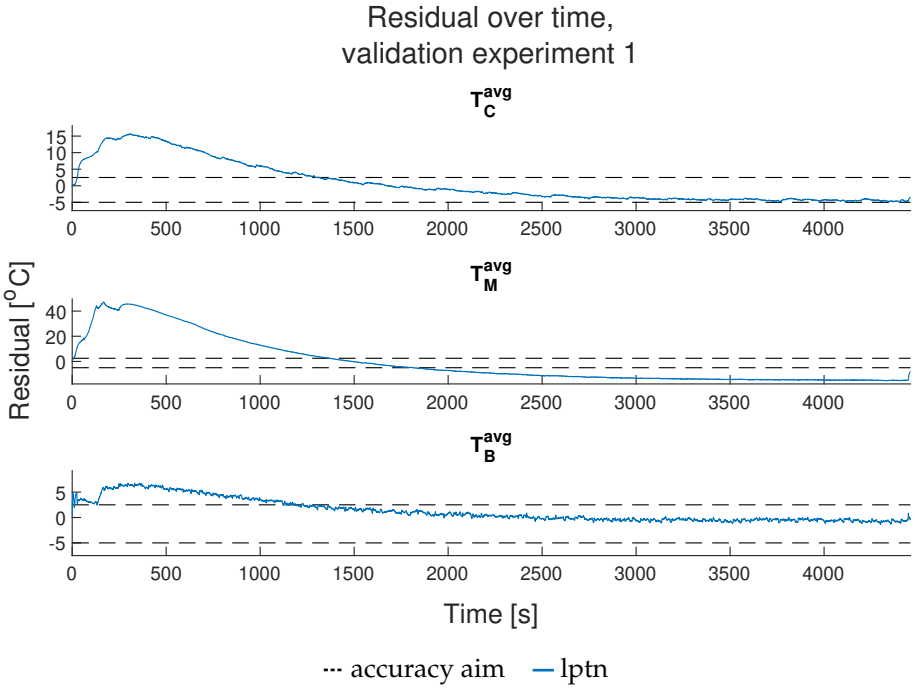

Figure 4.6: The residuals of the LPTN for validation experiment 1.

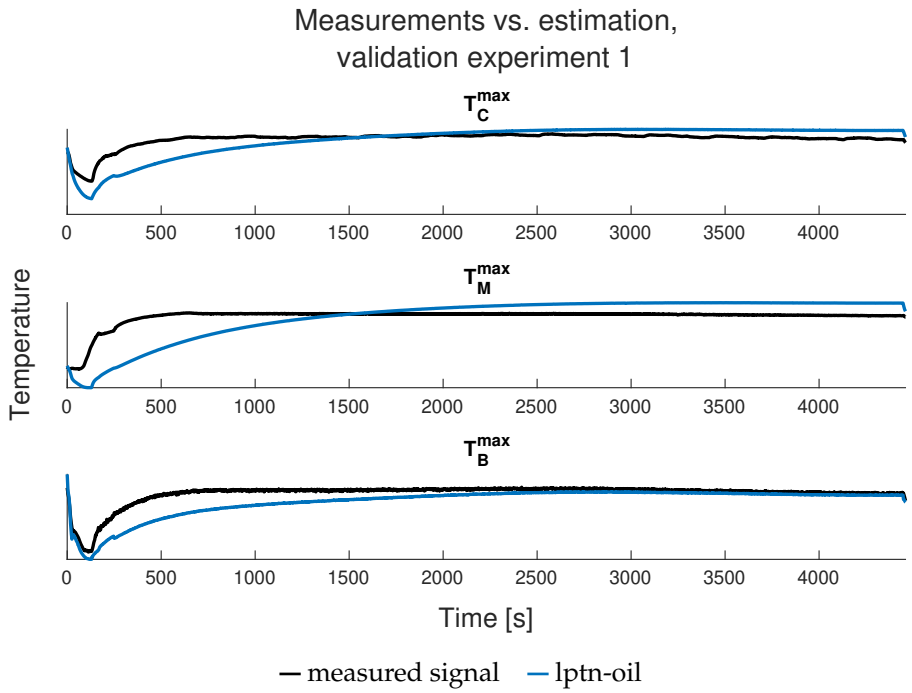

Figure 4.7: Comparison between validation experiment 1 and the simulated outputs of the LPTN-oil models.

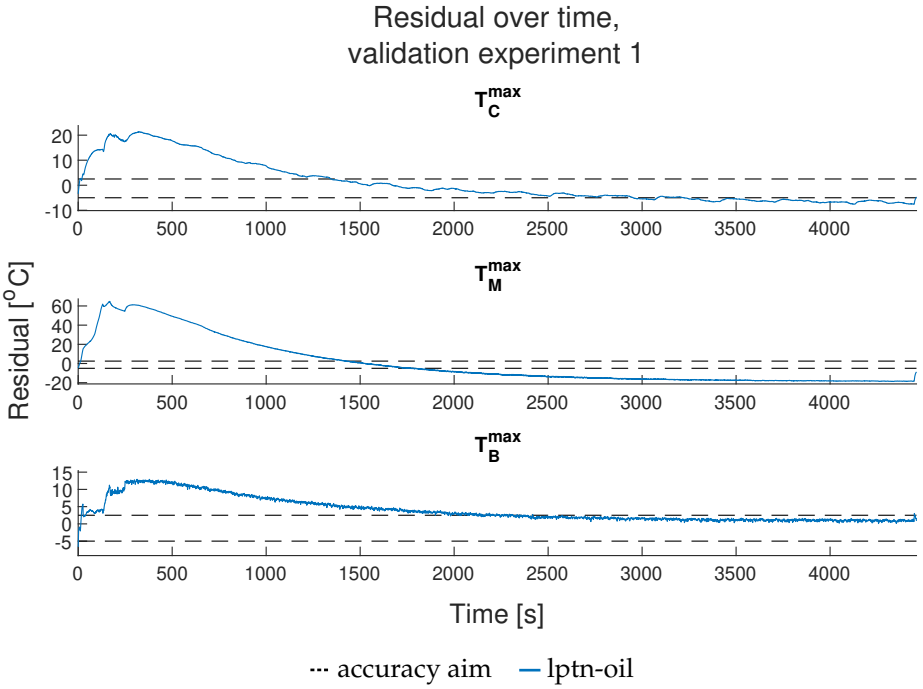

Figure 4.8: The residuals of the LPTN-oil models for validation experiment 1.

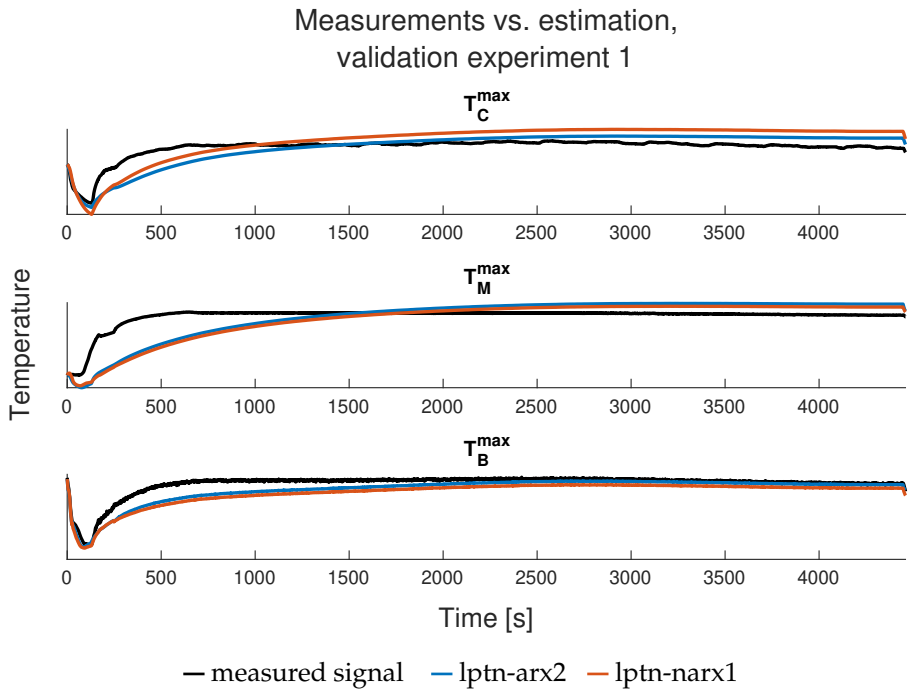

Figure 4.9: Comparison between validation experiment 1 and the simulated outputs of the LPTN-black-box models.

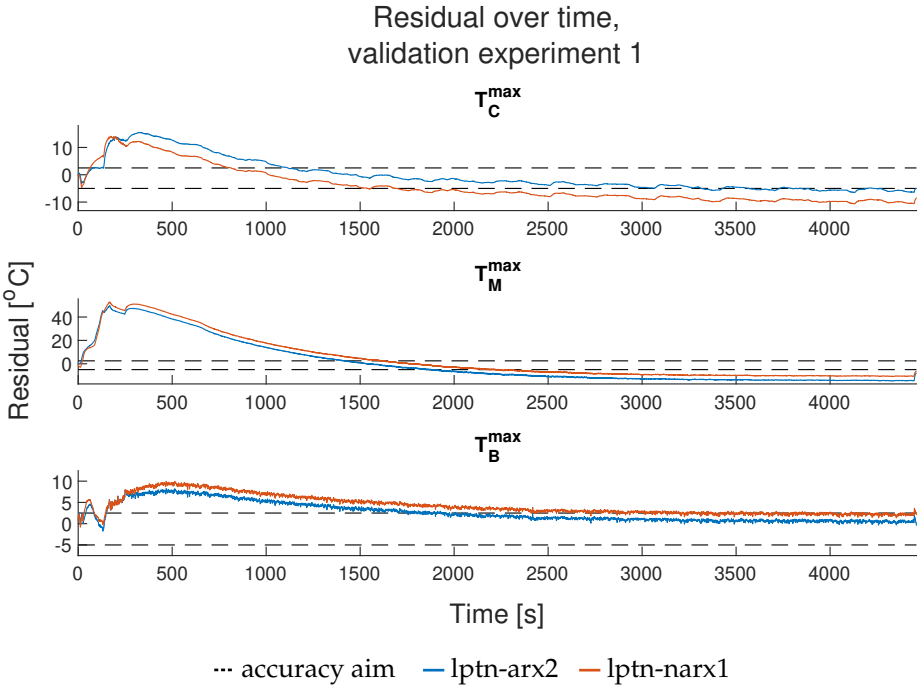

Figure 4.10: The residuals of the LPTN-black-box models for validation experiment 1.

Residual autocorrelation

The autocorrelation of residuals and the autocorrelation of residuals whose constant trend has been removed are shown here. Figure 4.11 and 4.12 concern the black-box models, Figure

4.13 and 4.14 the modified black-box models, Figure 4.15 and 4.16 the LPTN, Figure 4.17 and 4.18 the LPTN-oil models, and Figure 4.19 and 4.20 the LPTN-black-box models.

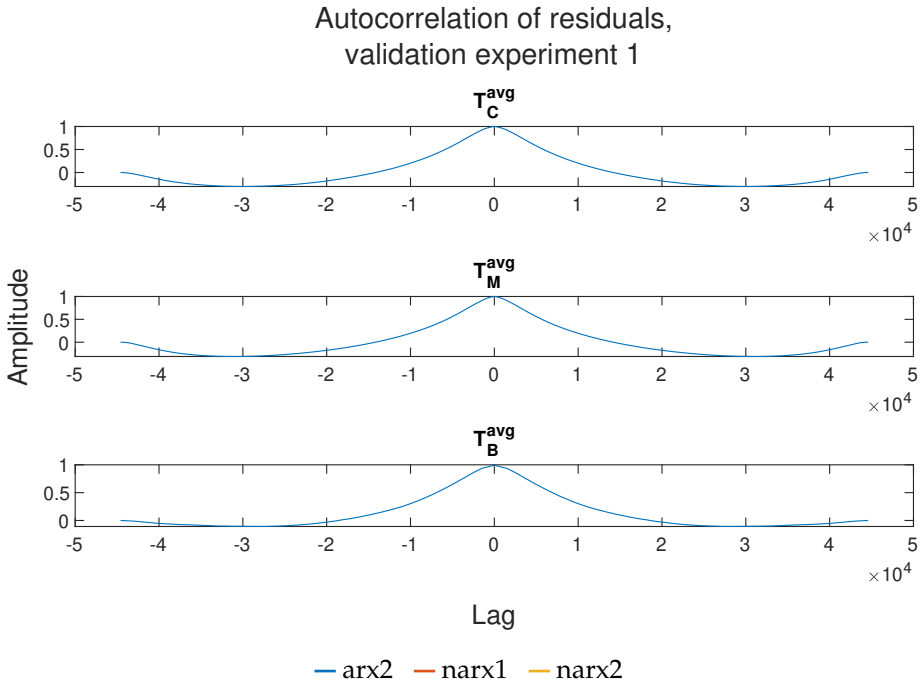

Figure 4.11: The residual autocorrelation of the black-box models for validation experiment 1.

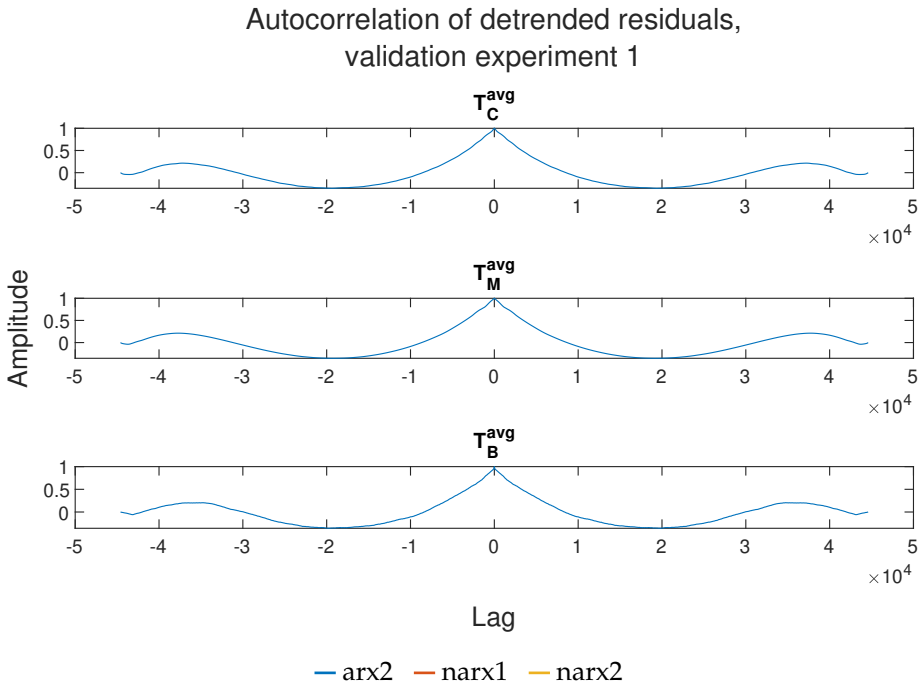

Figure 4.12: The detrended residual autocorrelation of the black-box models for validation experiment 1.

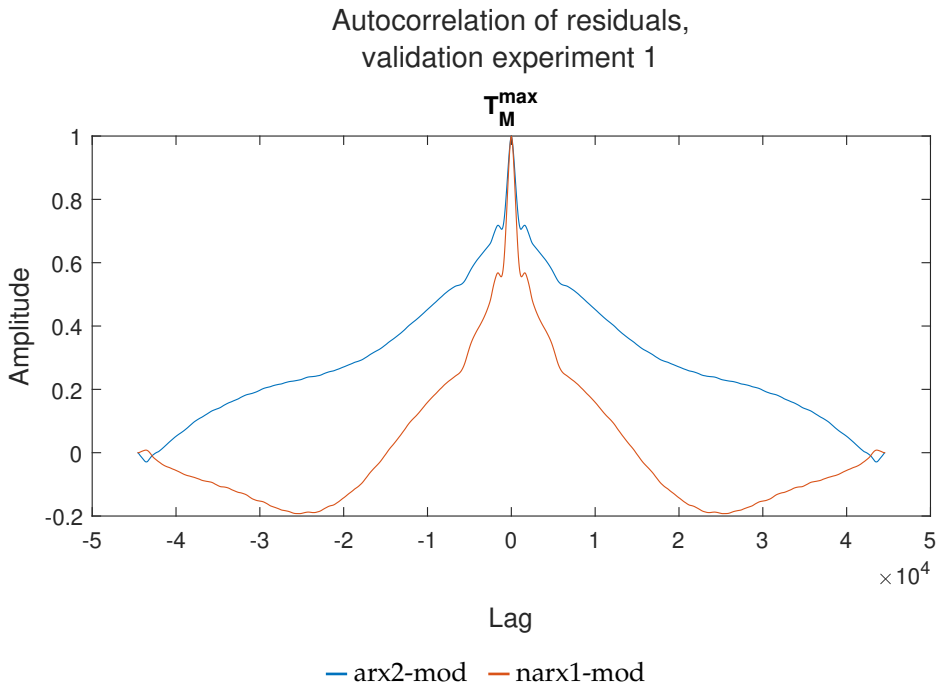

Figure 4.13: The residual autocorrelation of the modified black-box models for validation experiment 1.

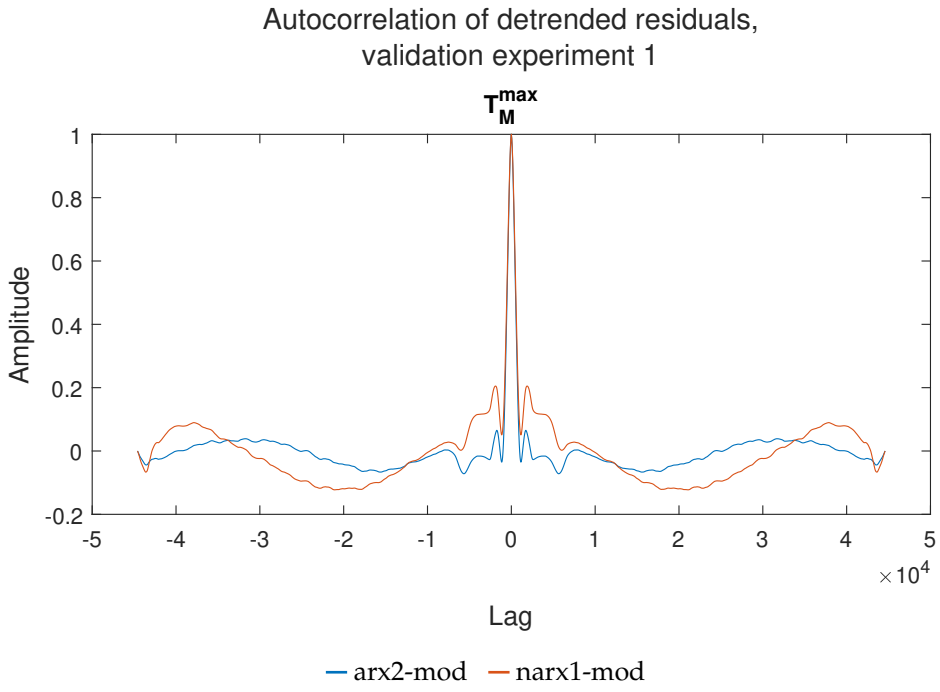

Figure 4.14: The detrended residual autocorrelation of the modified black-box models for validation experiment 1.

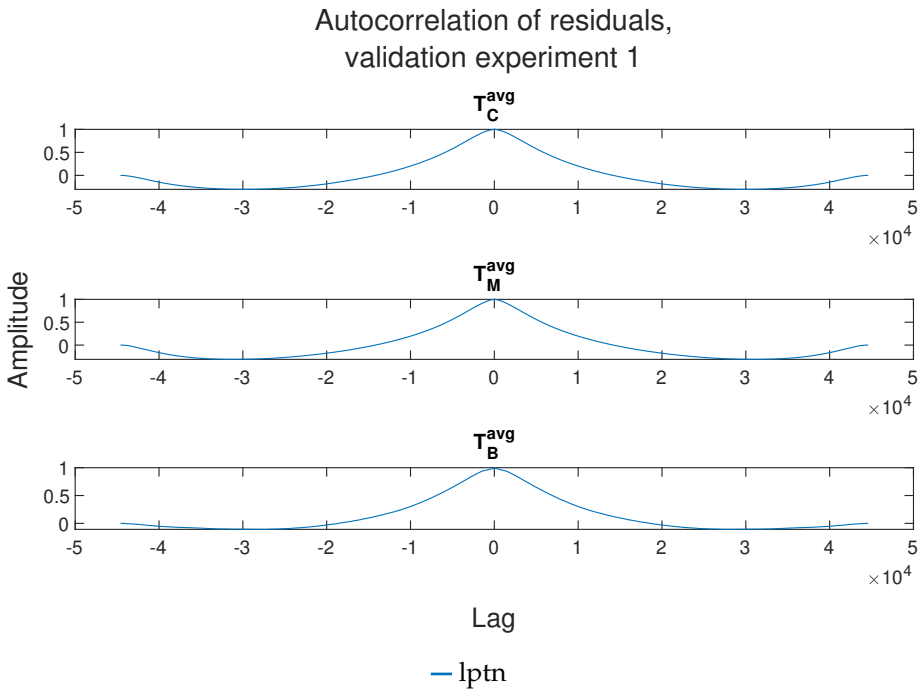

Figure 4.15: The residual autocorrelation of the LPTN for validation experiment 1.

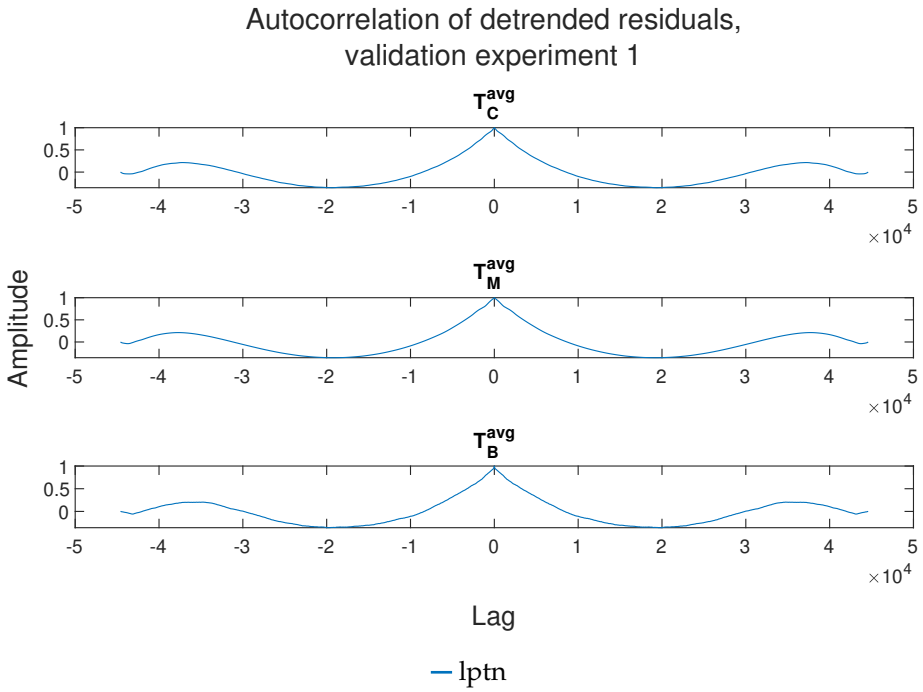

Figure 4.16: The detrended residual autocorrelation of the LPTN for validation experiment 1.

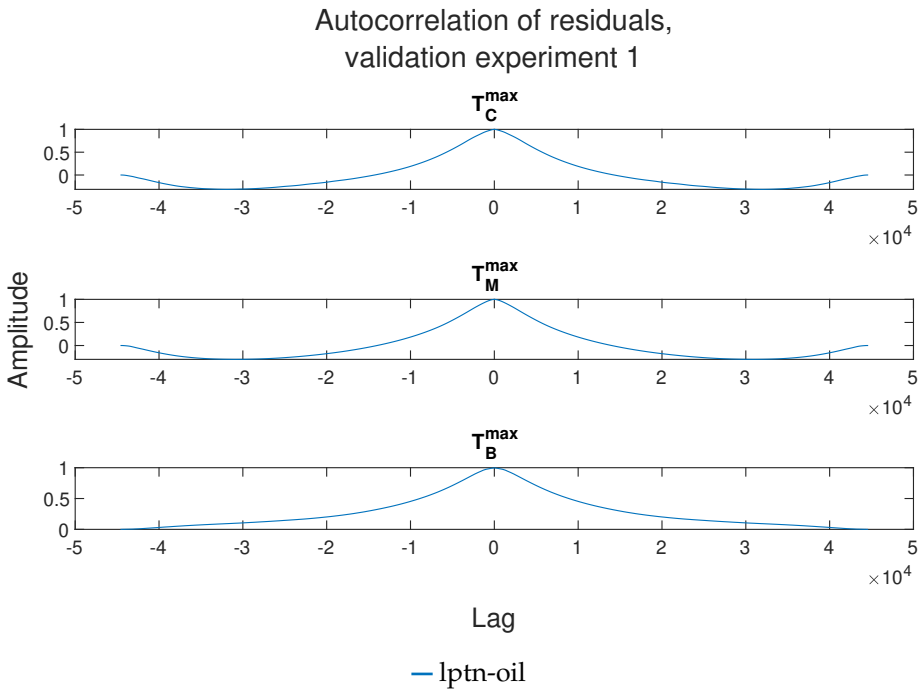

Figure 4.17: The residual autocorrelation of the LPTN-oil models for validation experiment 1.

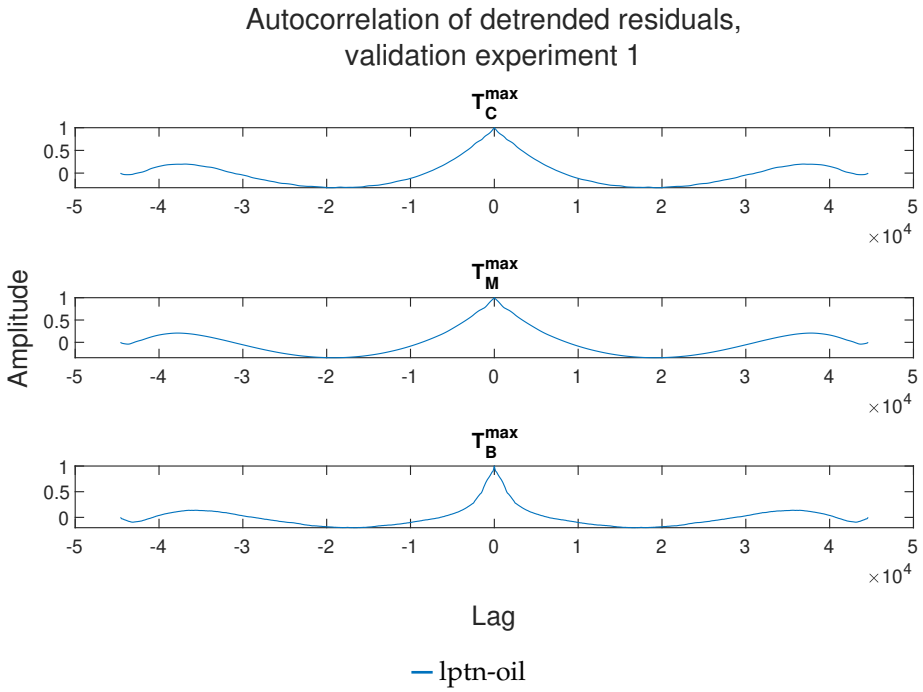

Figure 4.18: The detrended residual autocorrelation of the LPTN-oil models for validation experiment 1.

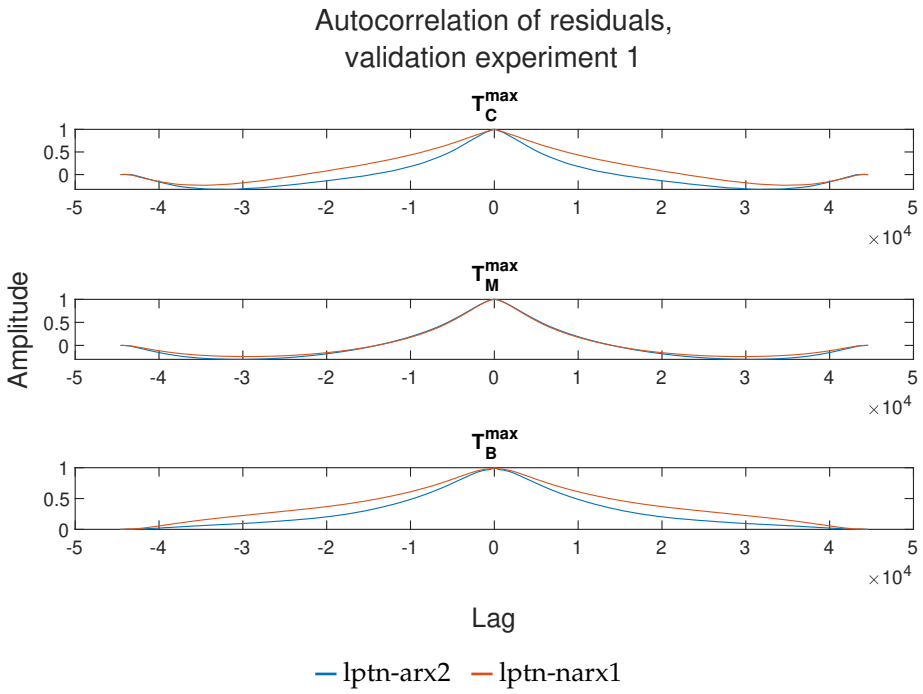

Figure 4.19: The residual autocorrelation of the LPTN-black-box models for validation experiment 1.

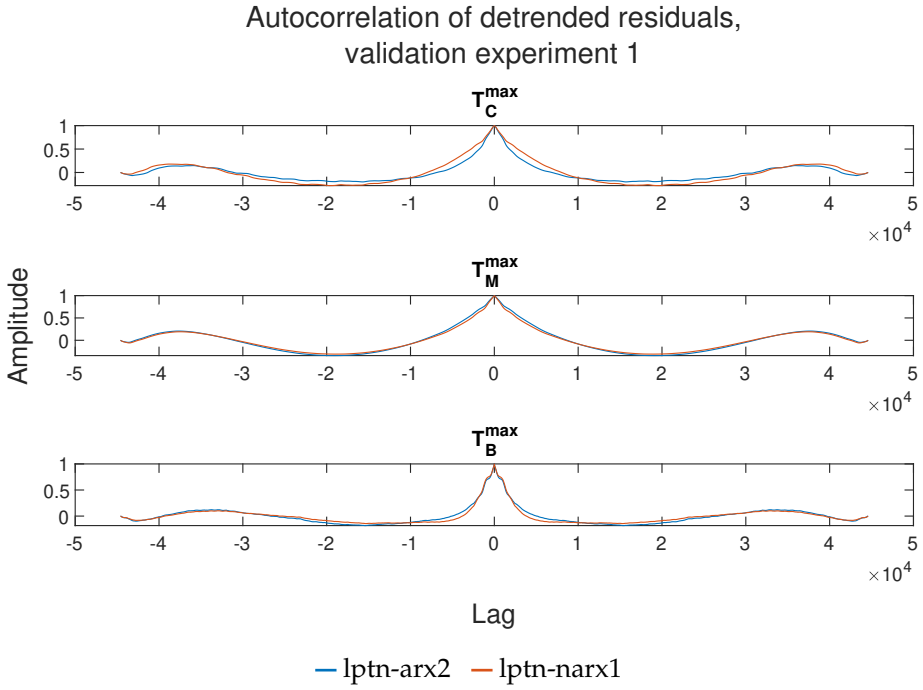

Figure 4.20: The detrended residual autocorrelation of the LPTN-black-box models for validation experiment 1.

Model fit percentages

Table 4.1 compares the fit percentages between the model outputs and the validation experiment. Note that the LPTN is evaluated against the average winding temperatures, and not the maximum as the other models are.

Table 4.1: Model fit percentages of the simulated model outputs for validation experiment 1. Values range between 100 and -∞ where 100 is the best possible fit.

	T_C	T_M	T_B
ARX2	48.24	53.10	31.86
NARX1	76.89	76.09	-3.68
NARX2	62.14	41.88	53.66
ARX2-Mod	-	60.66	-
NARX1-Mod	-	58.44	-
LPTN	-23.19	-72.86	30.72
LPTN-ARX2	6.13	-39.92	33.12
LPTN-NARX1	-17.27	-41.92	7.32
LPTN-Oil	-32.61	-80.49	-1.86

4.2 Validation experiment 2

The second validation experiment was also a step experiment. However, unlike validation experiment 1, this experiment started while the PMSM was at rest and the temperatures were close to ambient temperature. The temperature rise was therefore larger. Comparisons of measured and estimated temperatures and residual graphs are depicted below.

Output comparison

Figure 4.21 and 4.22 show temperature comparisons for the black-box models, Figure 4.23 and 4.24 for the modified black-box models, Figure 4.25 and 4.26 for the LPTN, Figure 4.27 and 4.28 for the LPTN and oil temperature combination, and lastly, Figure 4.29 and 4.30 for the LPTN-black-box models.

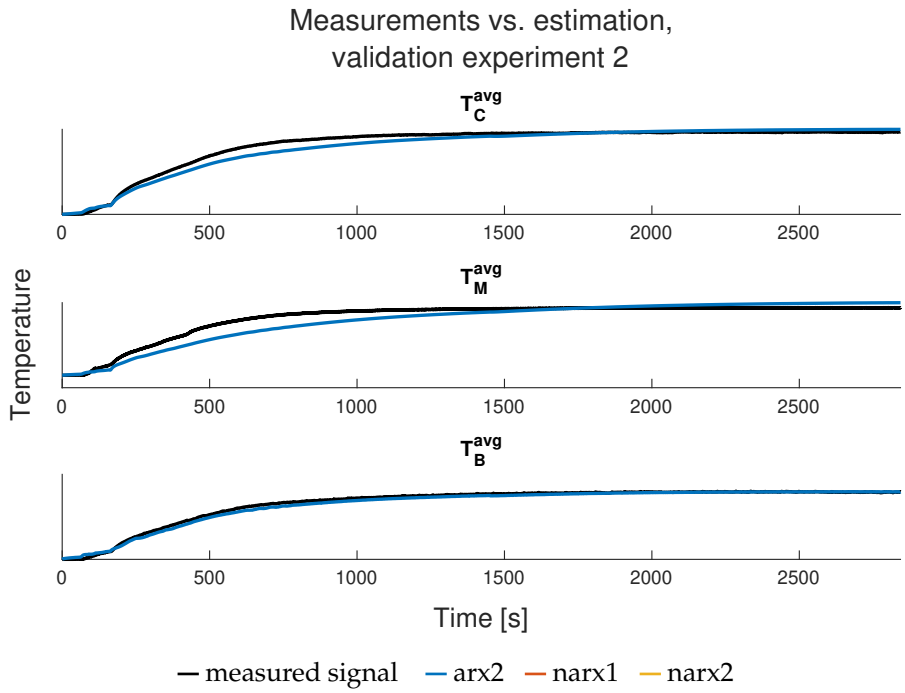

Figure 4.21: Comparison between validation experiment 2 and the simulated outputs of the black-box models.

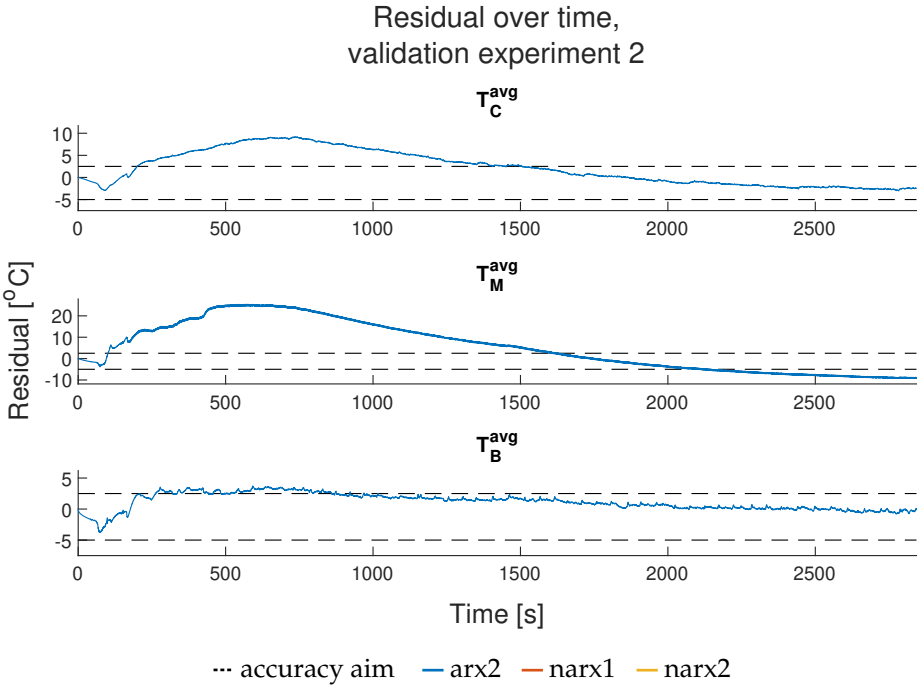

Figure 4.22: The residuals of the black-box models for validation experiment 2.

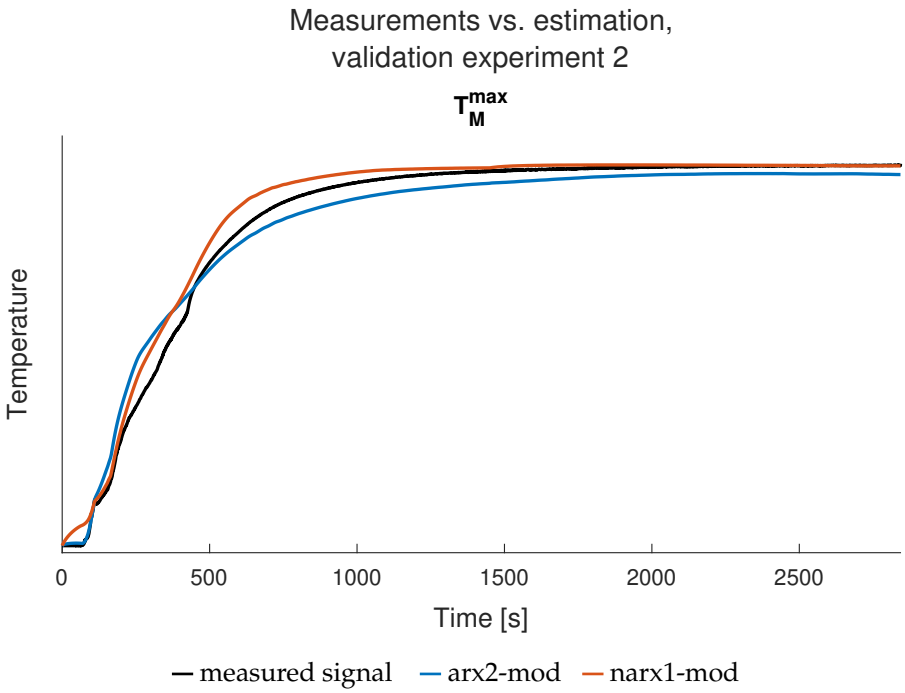

Figure 4.23: Comparison between validation experiment 2 and the simulated outputs of the modified black-box models.

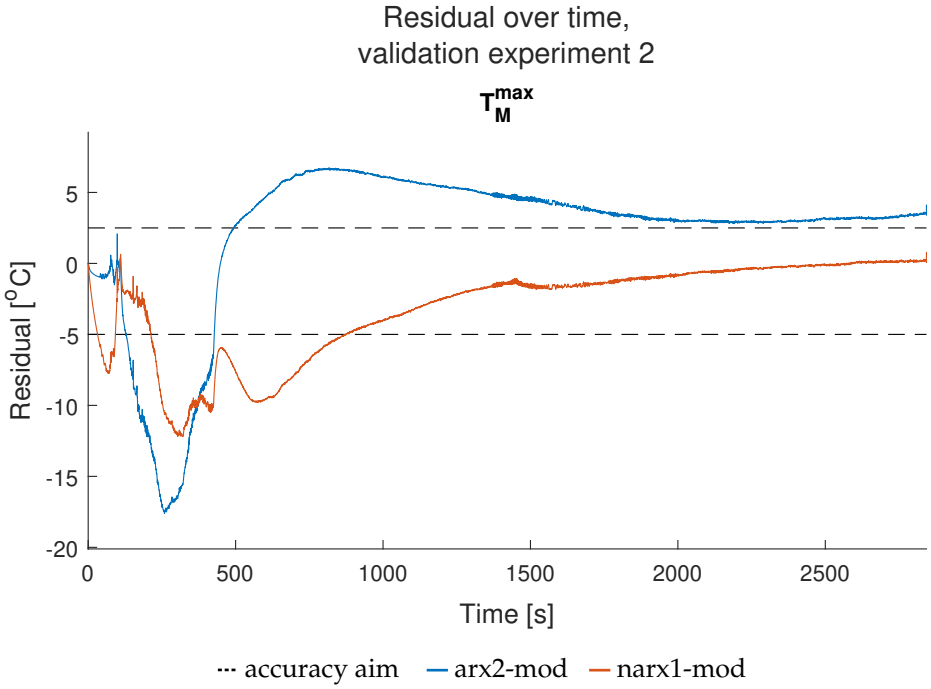

Figure 4.24: The residuals of the modified black-box models for validation experiment 2.

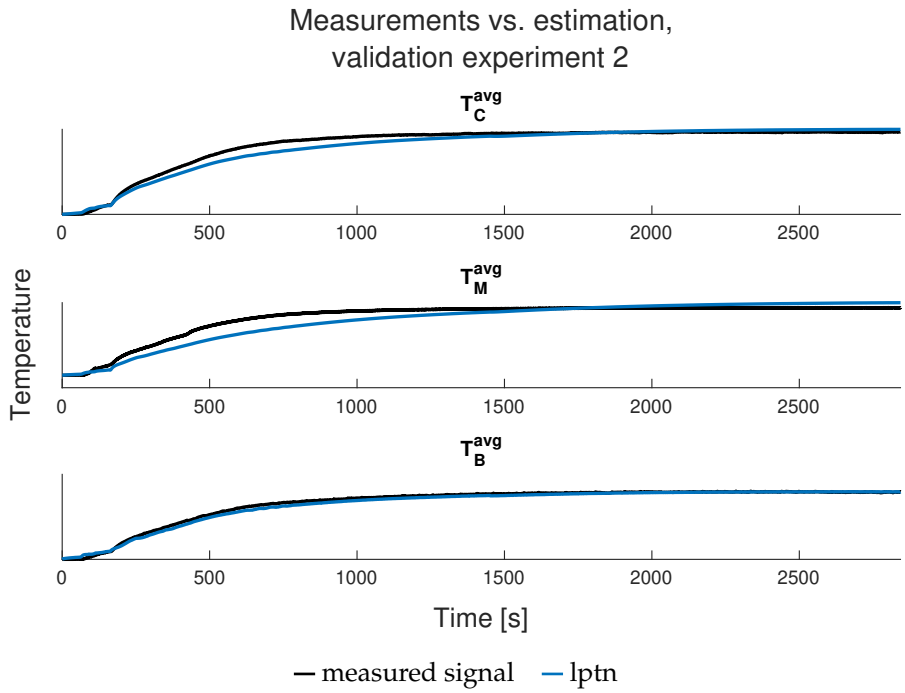

Figure 4.25: Comparison between validation experiment 2 and the simulated outputs of the LPTN.

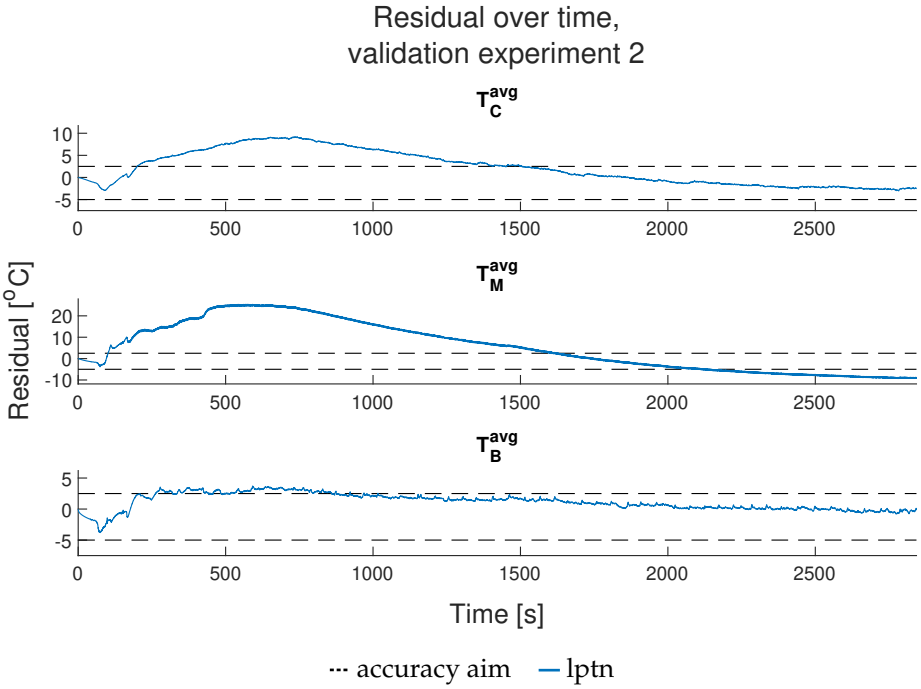

Figure 4.26: The residuals of the LPTN for validation experiment 2.

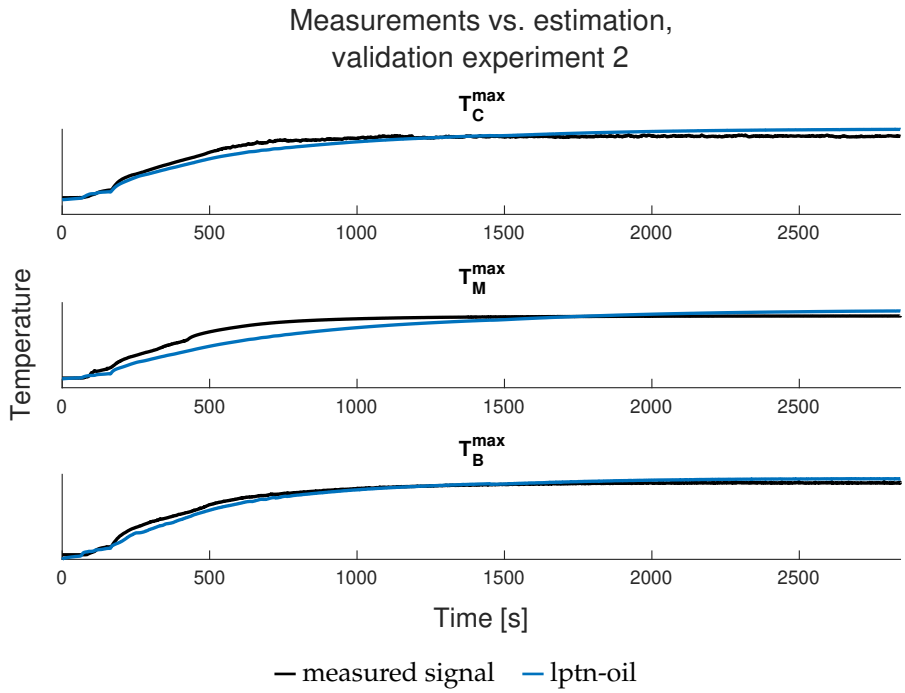

Figure 4.27: Comparison between validation experiment 2 and the simulated outputs of the LPTN-oil models.

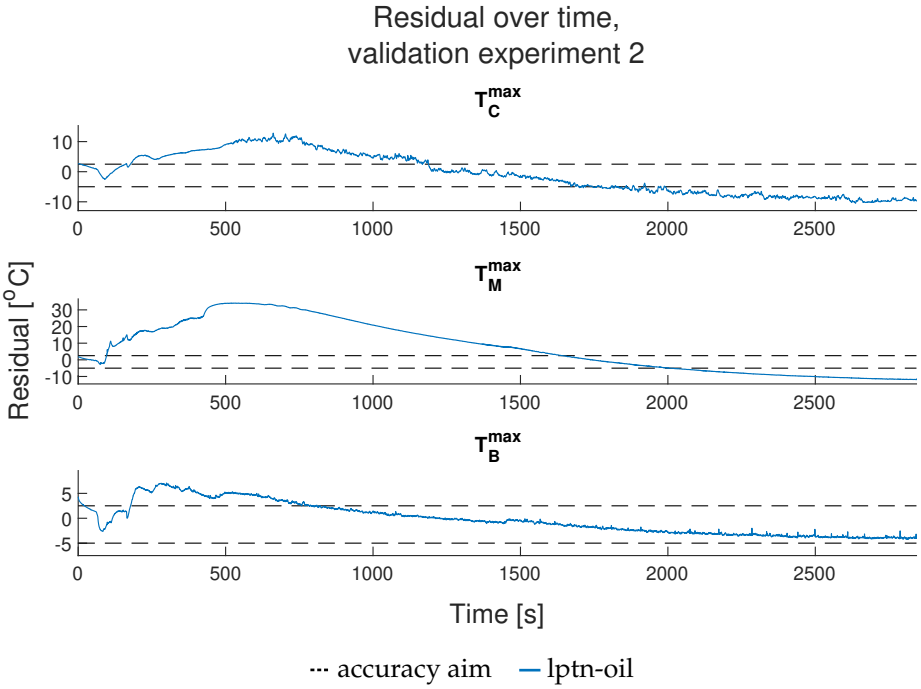

Figure 4.28: The residuals of the LPTN-oil models for validation experiment 2.

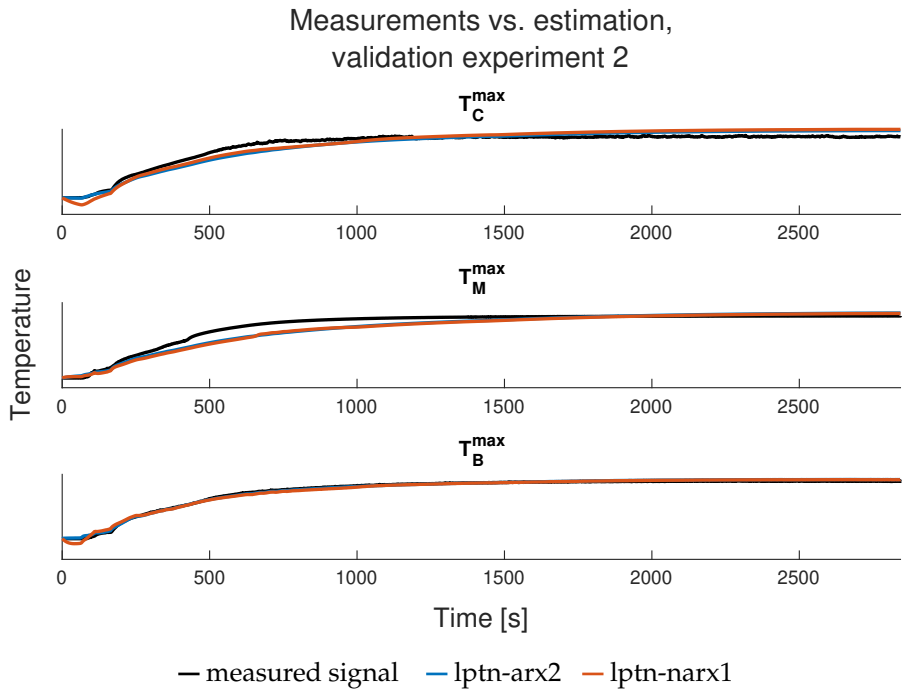

Figure 4.29: Comparison between validation experiment 2 and the simulated outputs of the LPTN-black-box models.

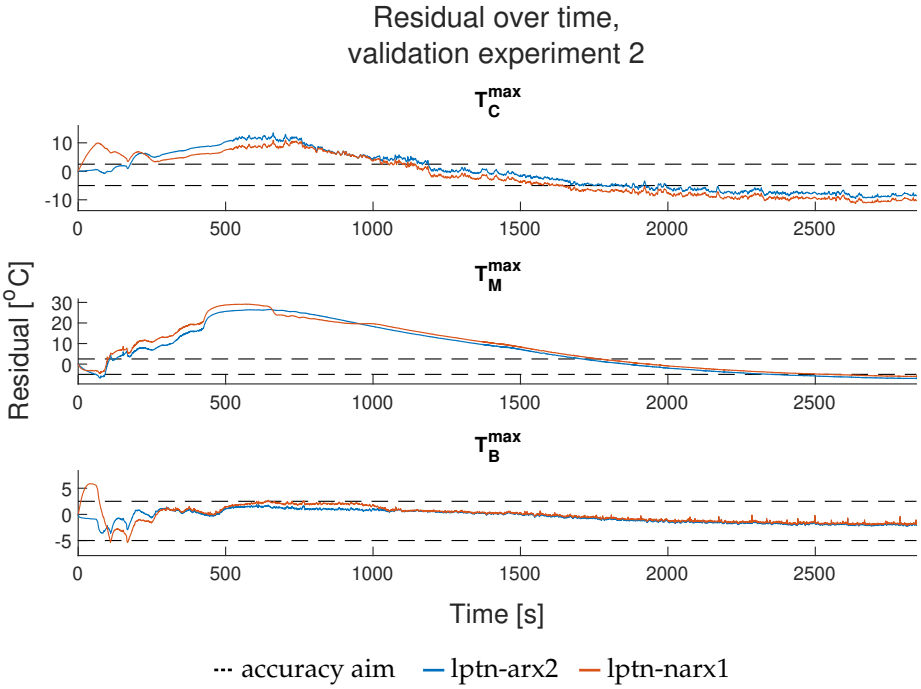

Figure 4.30: The residuals of the LPTN-black-box models for validation experiment 2.

Residual autocorrelation

The autocorrelation of residuals and the autocorrelation of residuals whose constant trend has been removed are shown here. Figure 4.31 and 4.32 concern the black-box models, Figure

4.33 and 4.34 the modified black-box models, Figure 4.35 and 4.36 the LPTN, Figure 4.37 and 4.38 the LPTN-oil models, and Figure 4.39 and 4.40 the LPTN-black-box models.

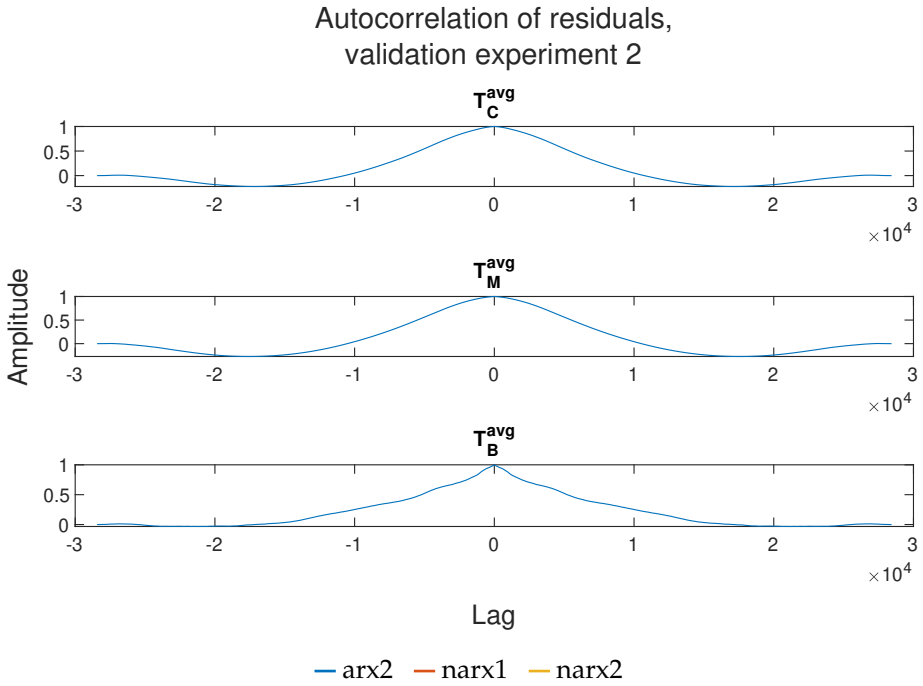

Figure 4.31: The residual autocorrelation of the black-box models for validation experiment 2.

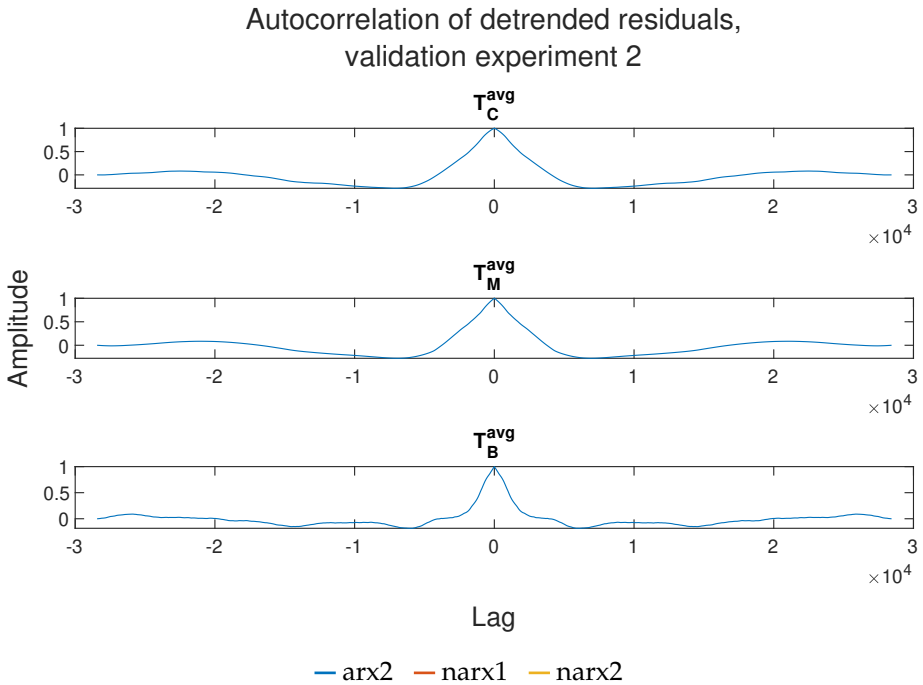

Figure 4.32: The detrended residual autocorrelation of the black-box models for validation experiment 2.

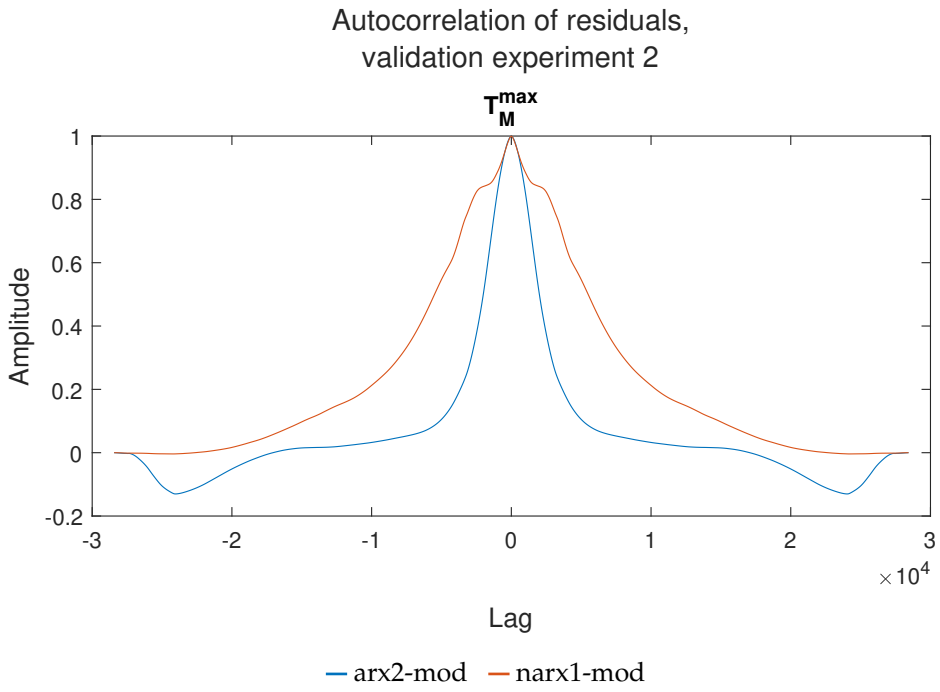

Figure 4.33: The residual autocorrelation of the modified black-box models for validation experiment 2.

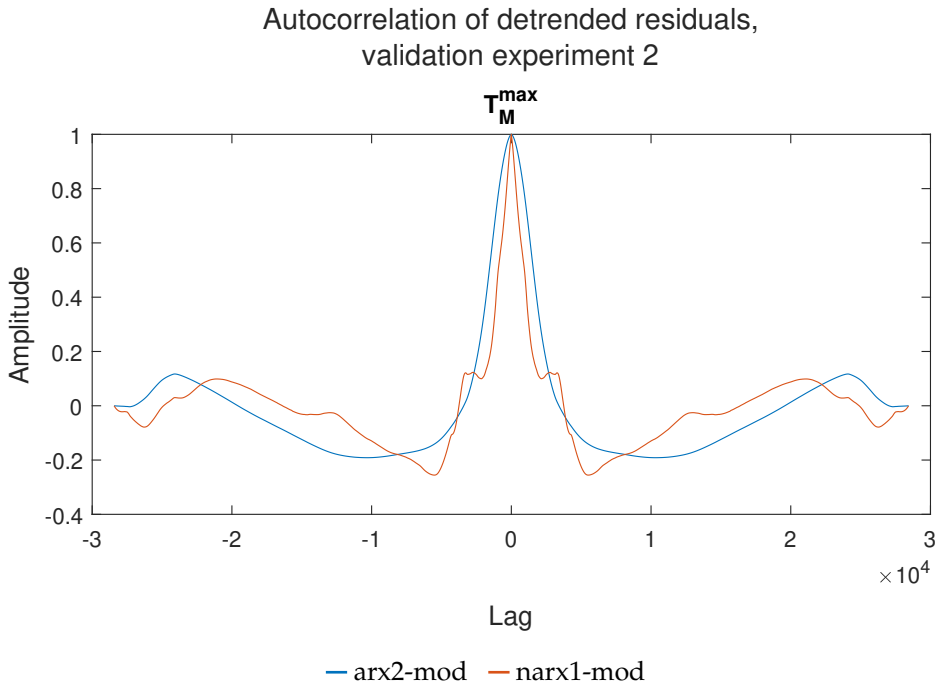

Figure 4.34: The detrended residual autocorrelation of the modified black-box models for validation experiment 2.

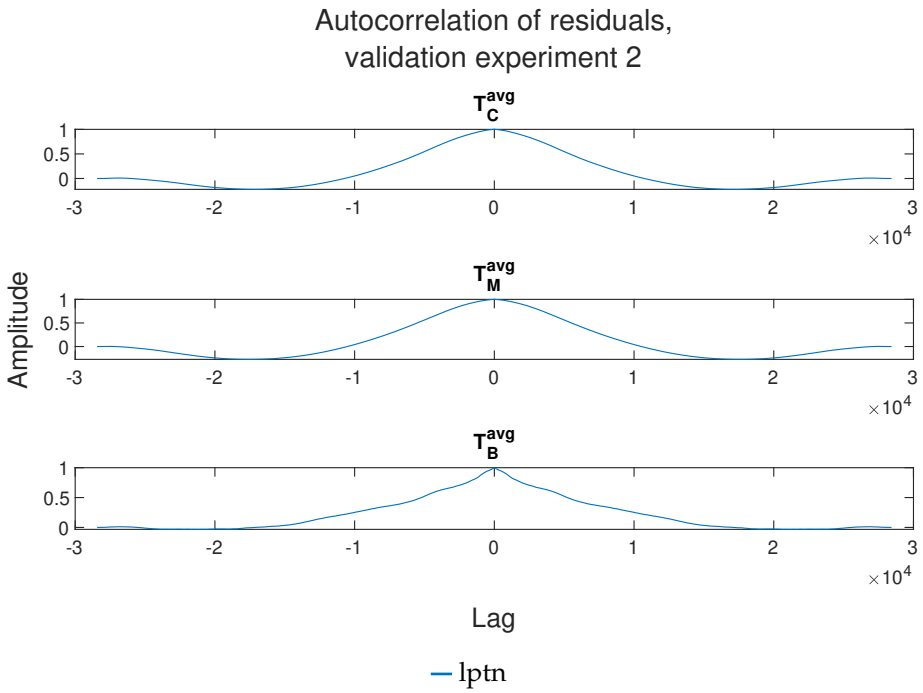

Figure 4.35: The residual autocorrelation of the LPTN for validation experiment 2.

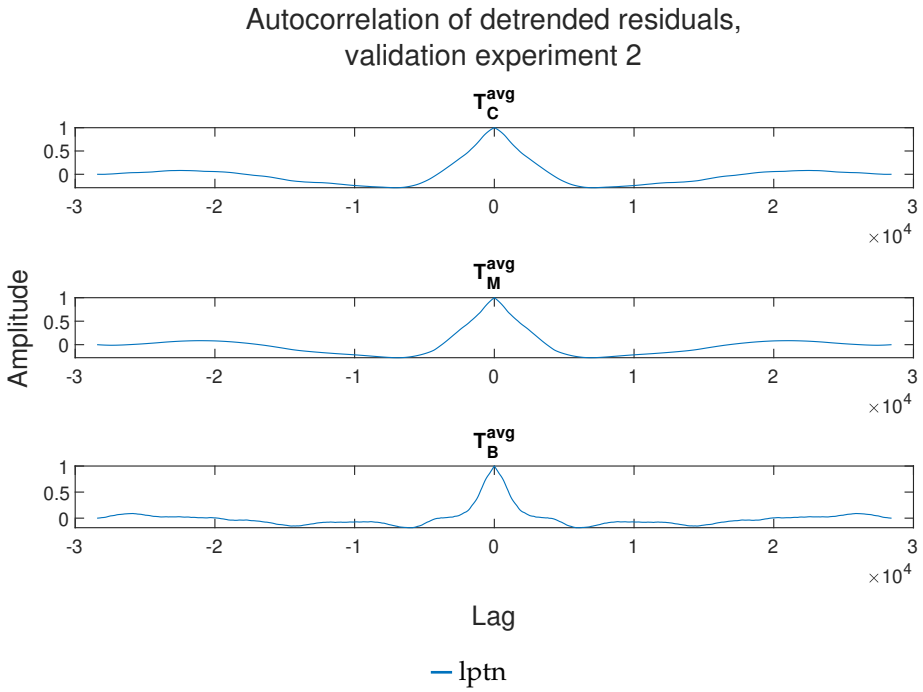

Figure 4.36: The detrended residual autocorrelation of the LPTN for validation experiment 2.

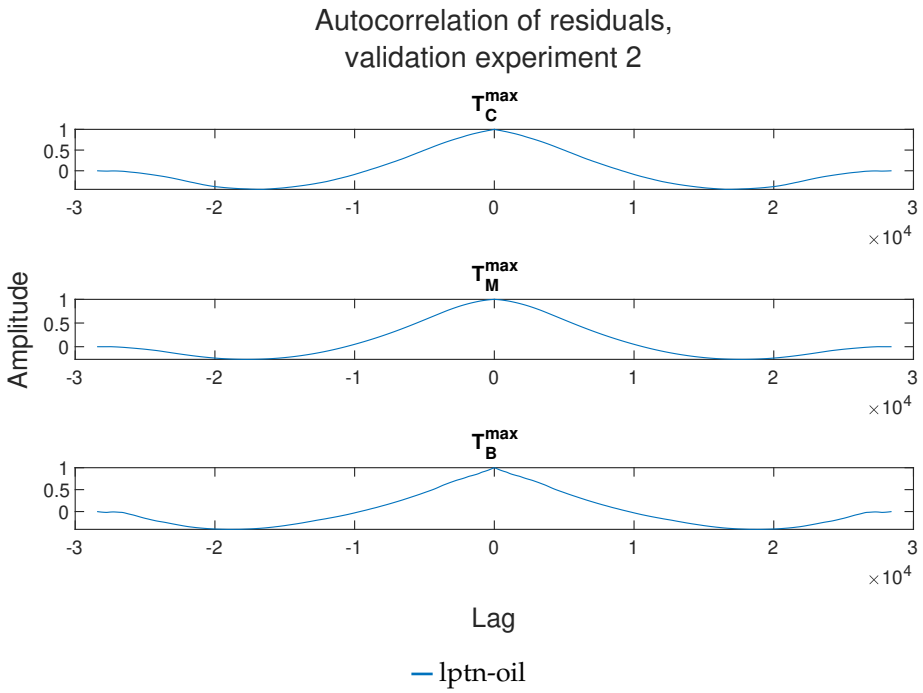

Figure 4.37: The residual autocorrelation of the LPTN-oil models for validation experiment 2.

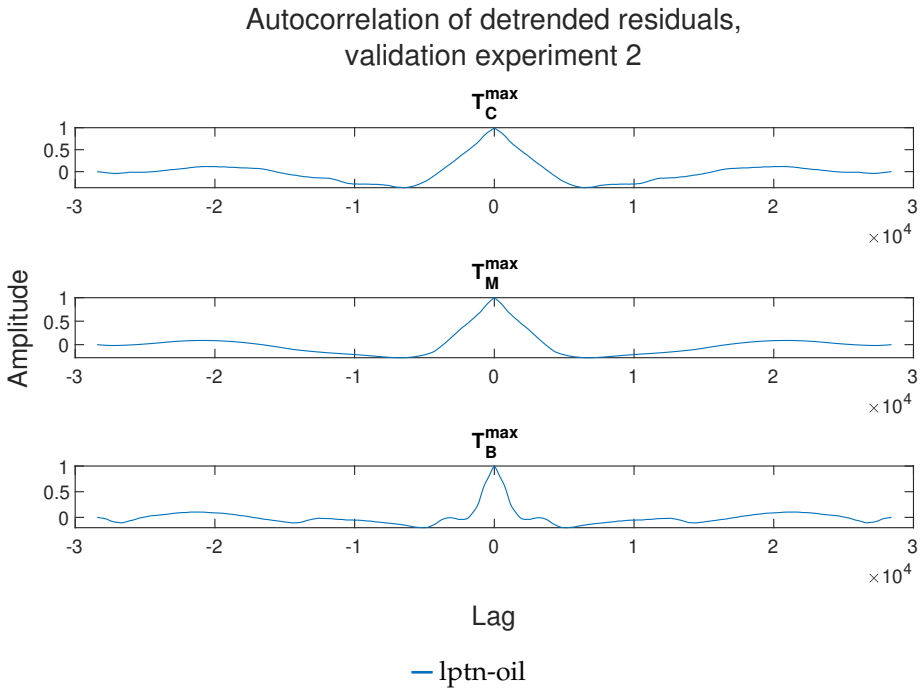

Figure 4.38: The detrended residual autocorrelation of the LPTN-oil models for validation experiment 2.

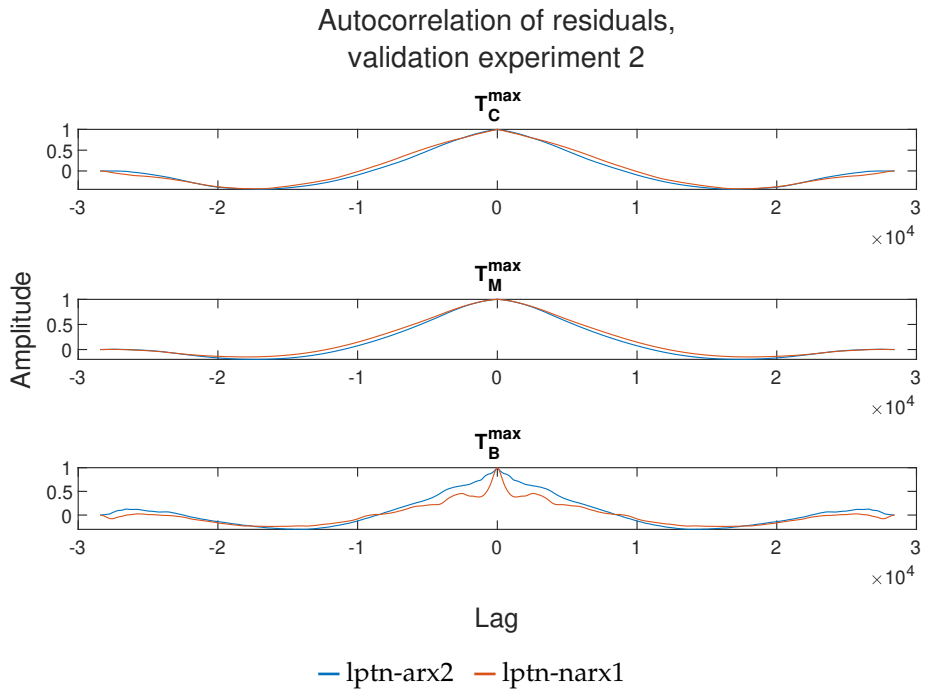

Figure 4.39: The residual autocorrelation of the LPTN-black-box models for validation experiment 2.

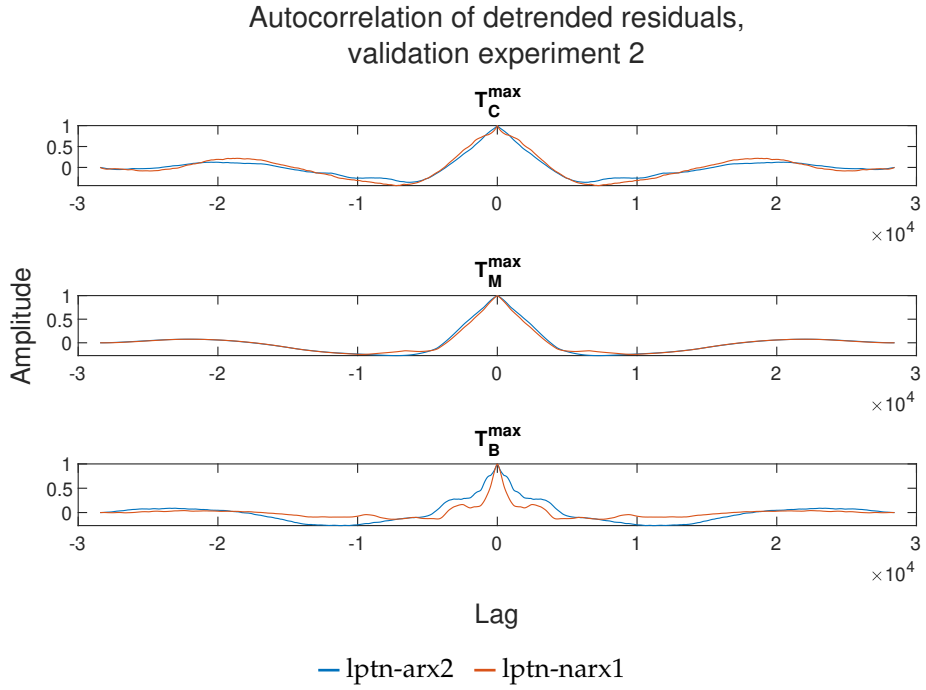

Figure 4.40: The detrended residual autocorrelation of the LPTN-black-box models for validation experiment 2.

Model fit percentages

Table 4.2 compares the fit percentages between the model outputs and the validation experiment. Note that the LPTN is evaluated against the average winding temperatures, and not the maximum as the other models are.

Table 4.2: Model fit percentages of the simulated model outputs for validation experiment 2. Values range between 100 and -∞ where 100 is the best possible fit.

	T_C	T_M	T_B
ARX2	84.73	85.17	88.33
NARX1	85.44	88.27	81.87
NARX2	88.57	85.99	93.96
ARX2-Mod	-	85.12	-
NARX1-Mod	-	89.13	-
LPTN	78.32	60.67	89.25
LPTN-ARX2	70.59	66.18	92.97
LPTN-NARX1	68.49	64.61	90.75
LPTN-Oil	70.15	56.10	82.33

4.3 Validation experiment 3

The third and last validation experiment was a drive cycle experiment with highly varying data. Comparisons of measured and estimated temperatures and residual graphs are illustrated below.

Output comparison

Figure 4.41 and 4.42 show temperature comparisons for the black-box models, Figure 4.43 and 4.44 for the modified black-box models, Figure 4.45 and 4.46 for the LPTN, Figure 4.47 and 4.48 for the LPTN and oil temperature combination, and lastly, Figure 4.49 and 4.50 for the LPTN-black-box models.

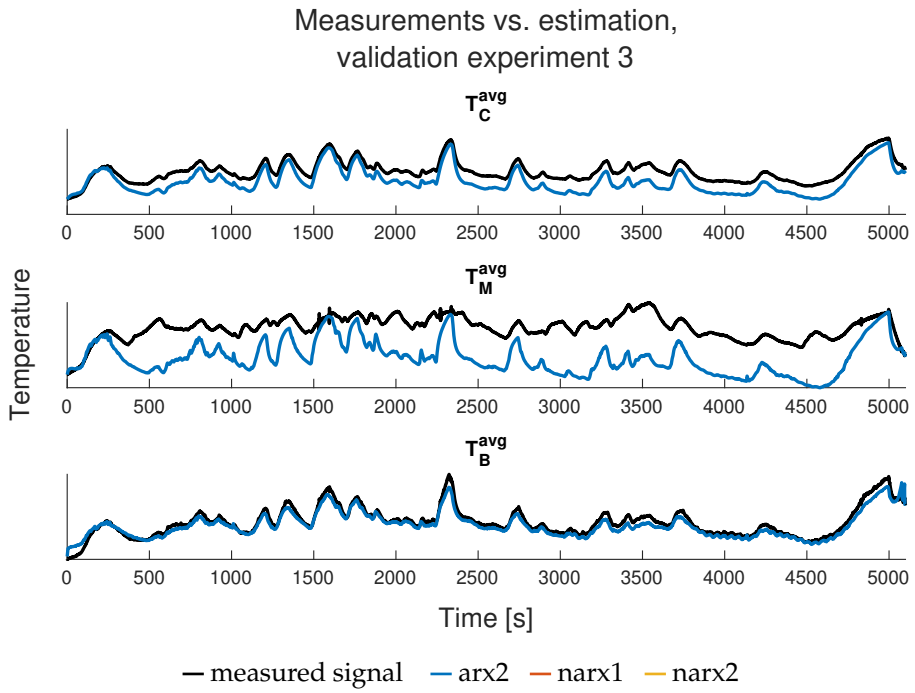

Figure 4.41: Comparison between validation experiment 3 and the simulated outputs of the black-box models.

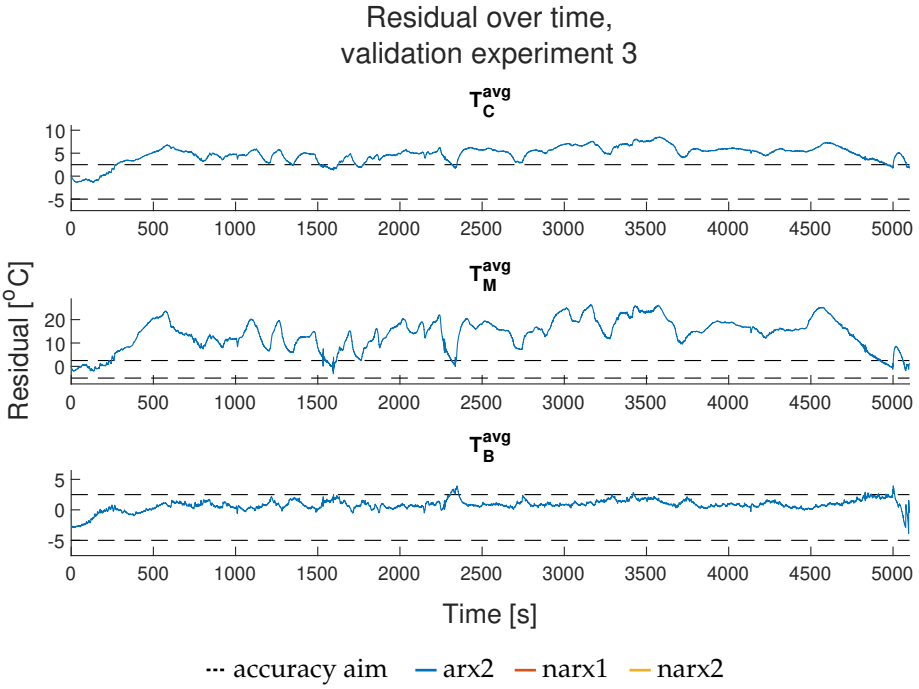

Figure 4.42: The residuals of the black-box models for validation experiment 3.

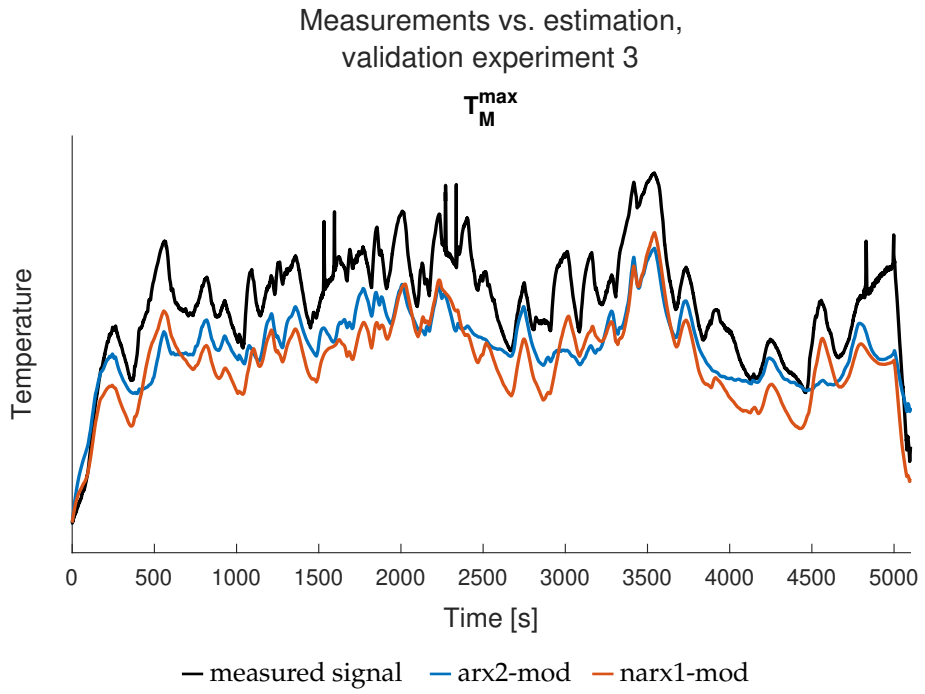

Figure 4.43: Comparison between validation experiment 3 and the simulated outputs of the modified black-box models.

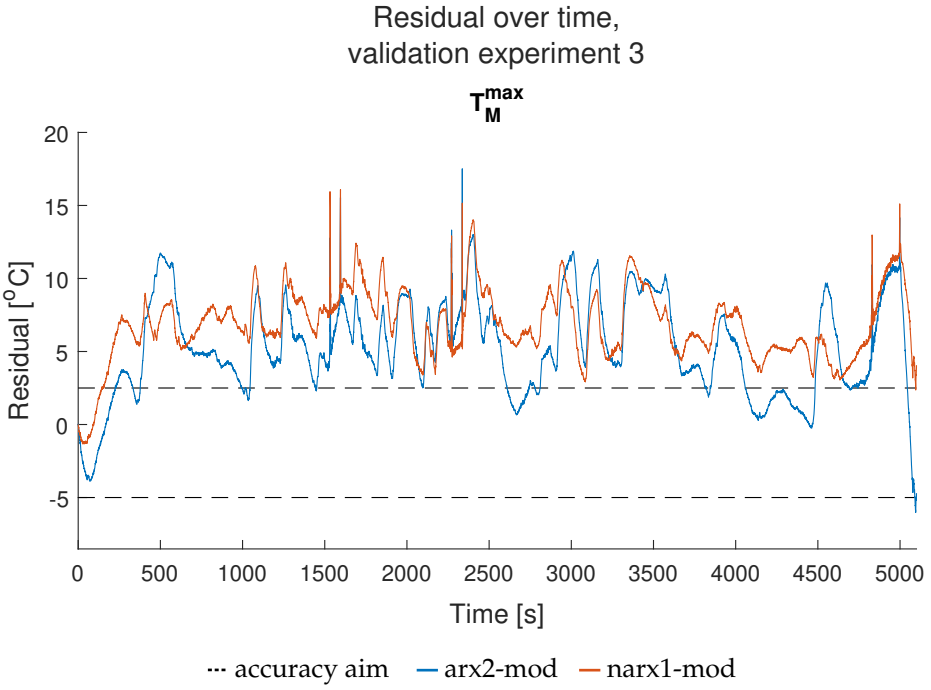

Figure 4.44: The residuals of the modified black-box models for validation experiment 3.

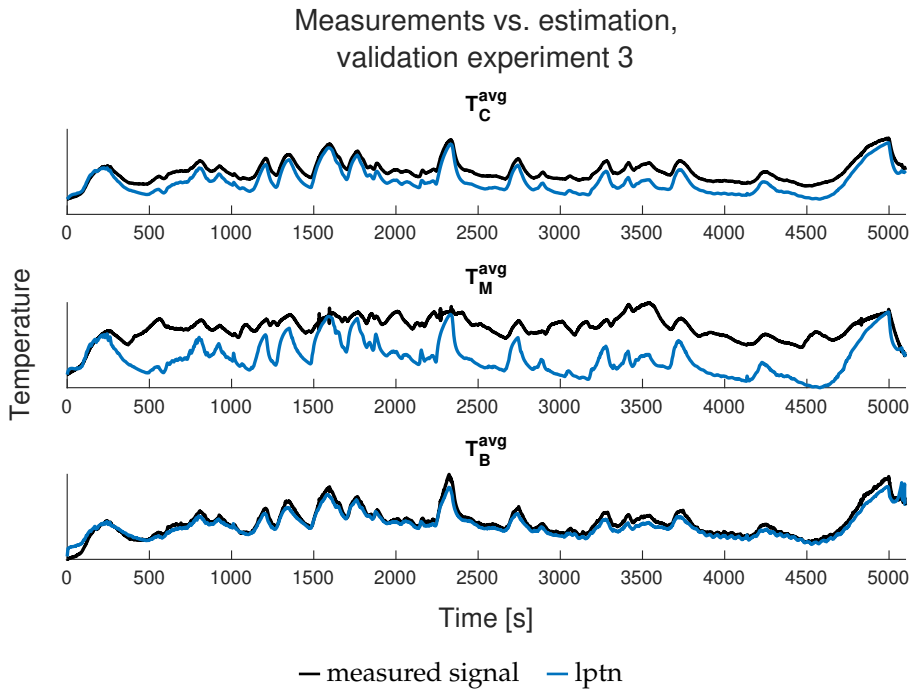

Figure 4.45: Comparison between validation experiment 3 and the simulated outputs of the LPTN.

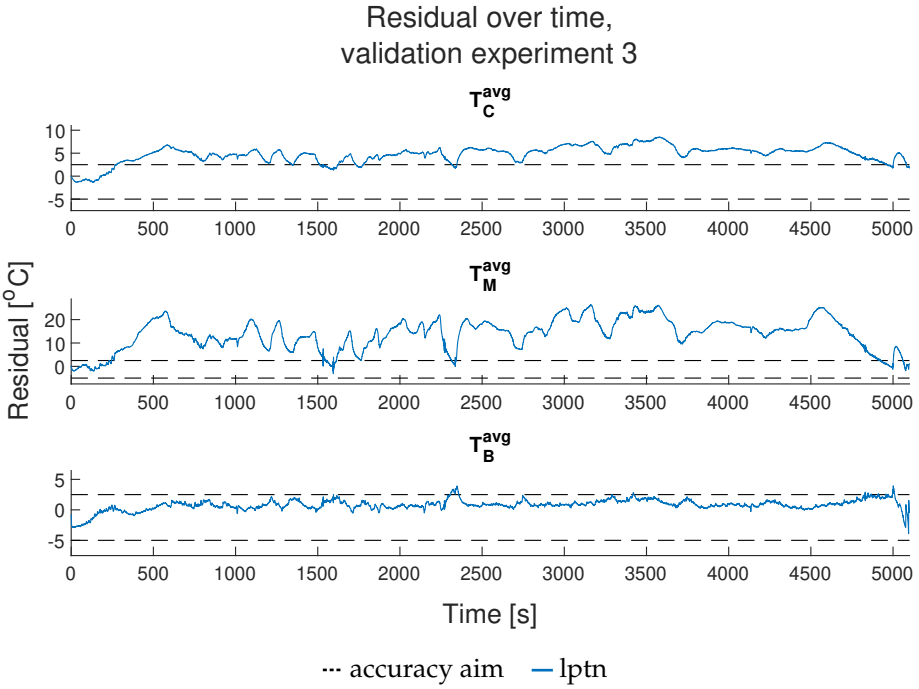

Figure 4.46: The residuals of the LPTN for validation experiment 3.

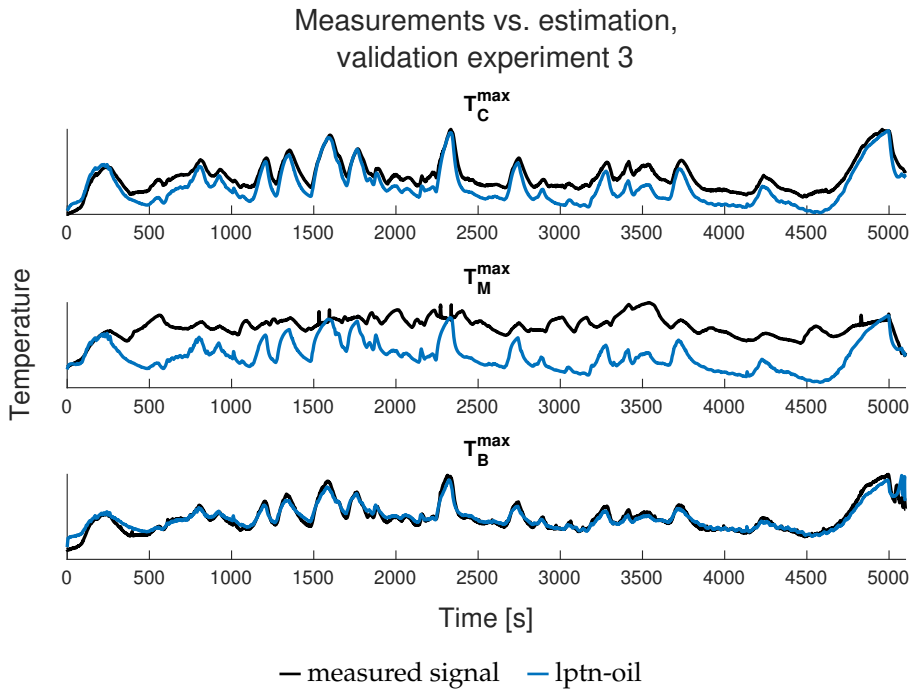

Figure 4.47: Comparison between validation experiment 3 and the simulated outputs of the LPTN-oil models.

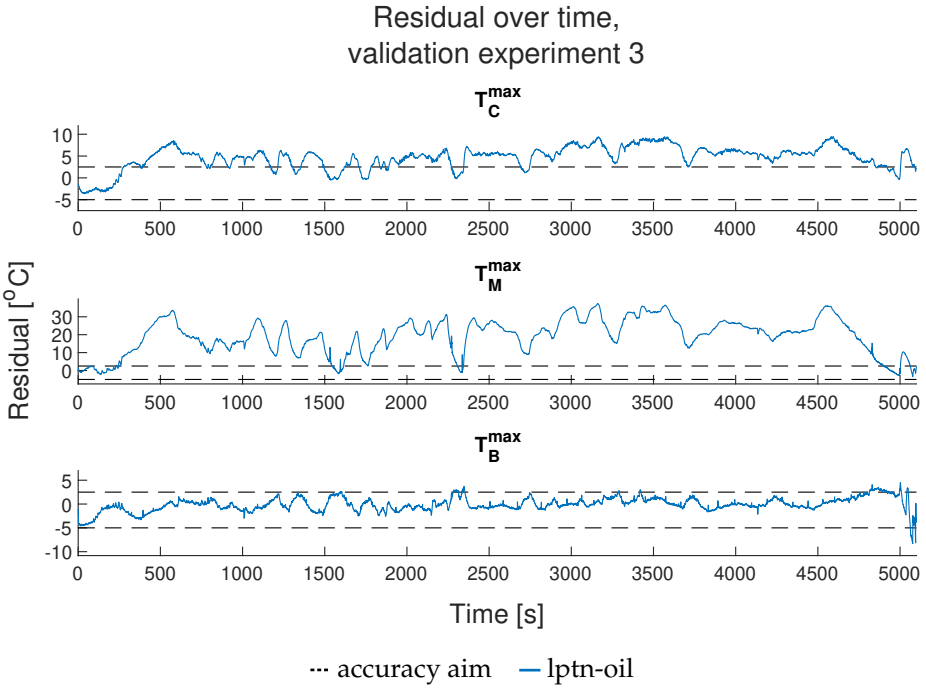

Figure 4.48: The residuals of the LPTN-oil models for validation experiment 3.

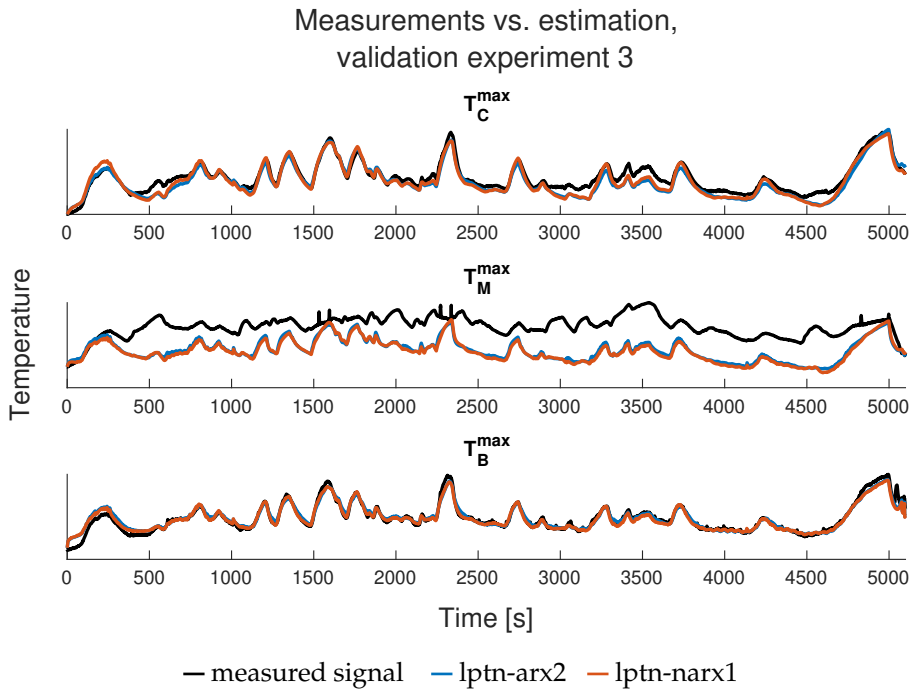

Figure 4.49: Comparison between validation experiment 3 and the simulated outputs of the LPTN-black-box models.

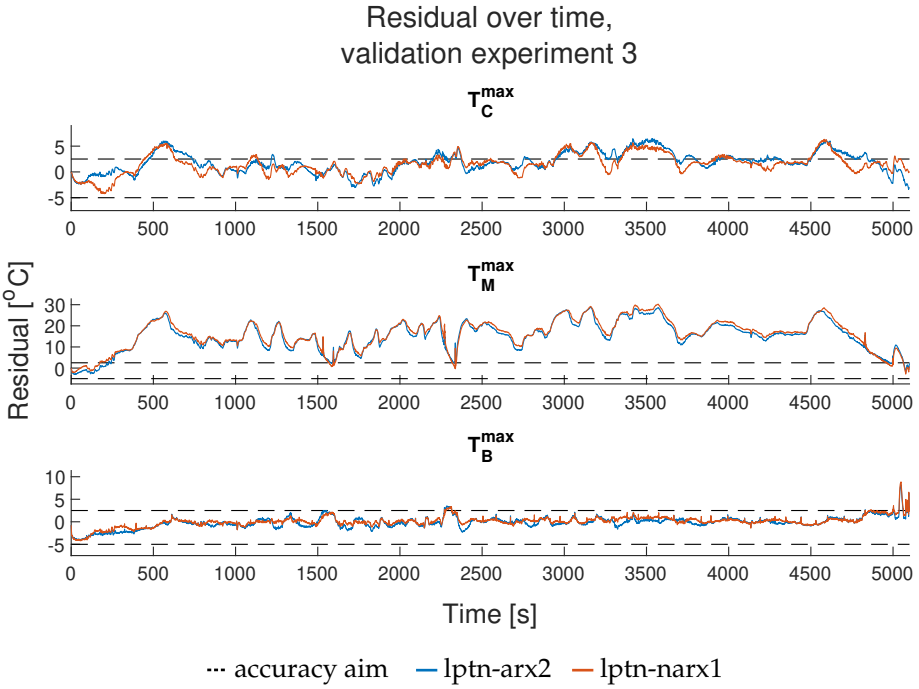

Figure 4.50: The residuals of the LPTN-black-box models for validation experiment 3.

Residual autocorrelation

The autocorrelation of residuals and the autocorrelation of residuals whose constant trend has been removed are shown here. Figure 4.51 and 4.52 concern the black-box models, Figure

4.53 and 4.54 the modified black-box models, Figure 4.55 and 4.56 the LPTN, Figure 4.57 and 4.58 the LPTN-oil models, and Figure 4.59 and 4.60 the LPTN-black-box models.

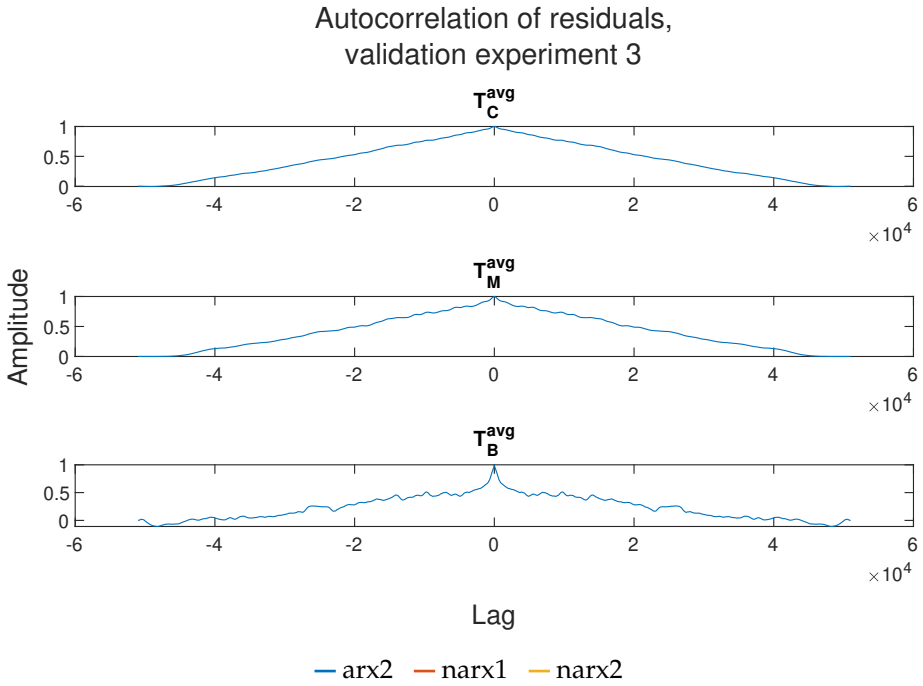

Figure 4.51: The residual autocorrelation of the black-box models for validation experiment 3.

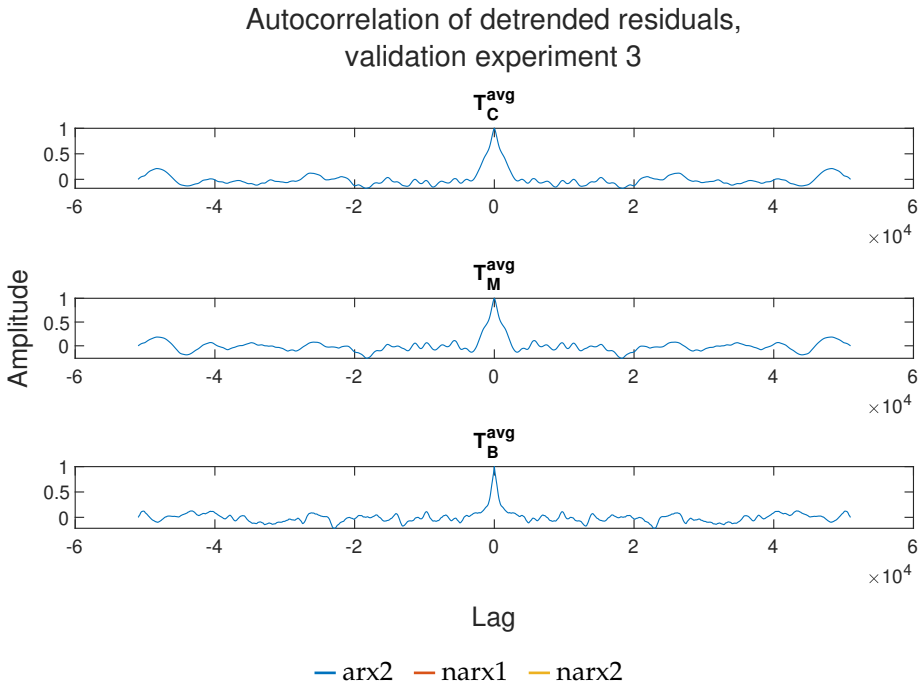

Figure 4.52: The detrended residual autocorrelation of the black-box models for validation experiment 3.

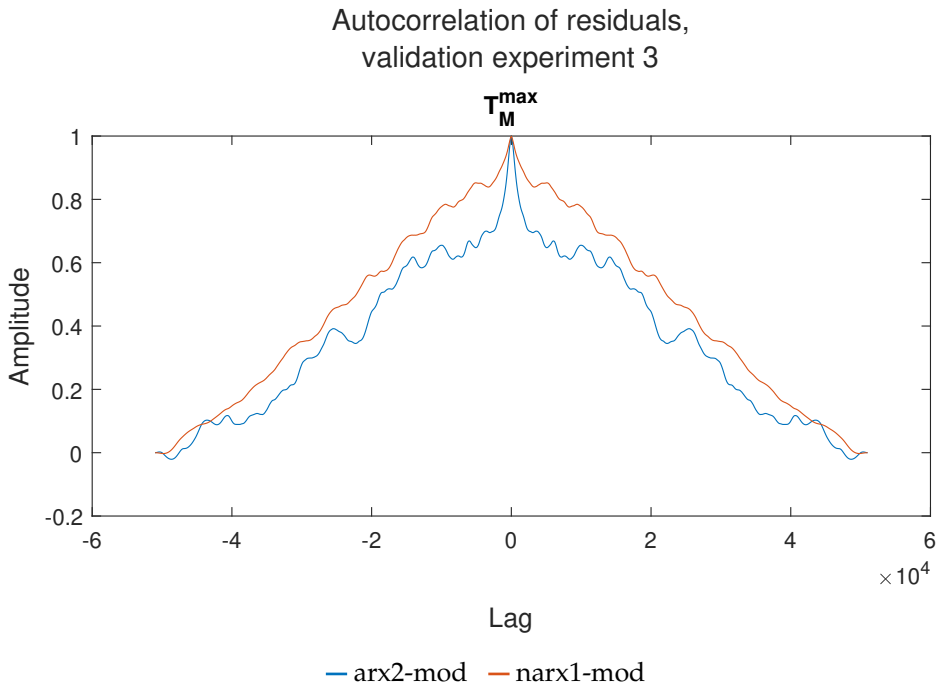

Figure 4.53: The residual autocorrelation of the modified black-box models for validation experiment 3.

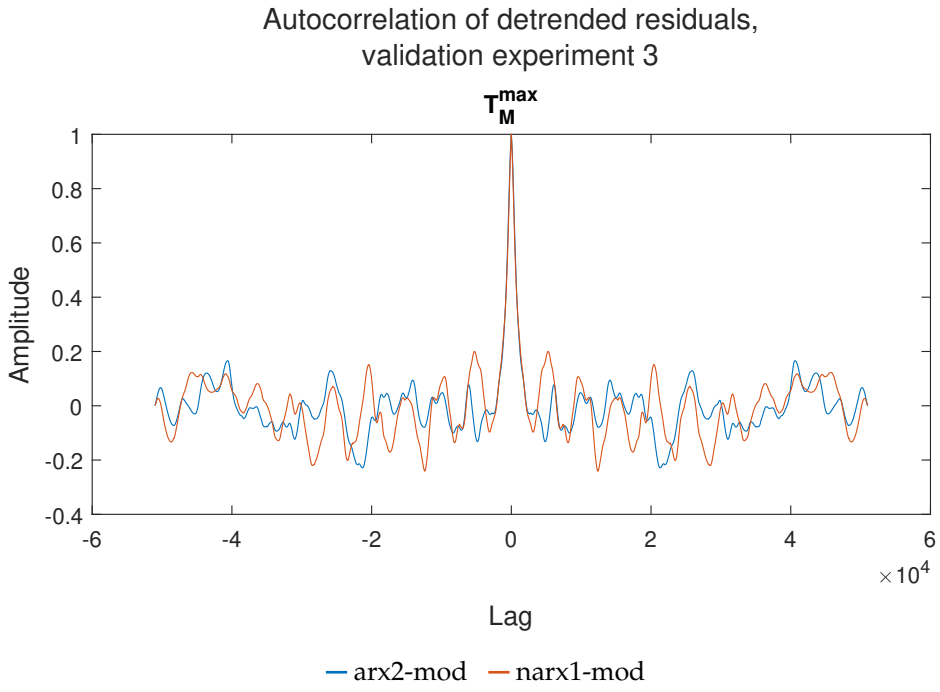

Figure 4.54: The detrended residual autocorrelation of the modified black-box models for validation experiment 3.

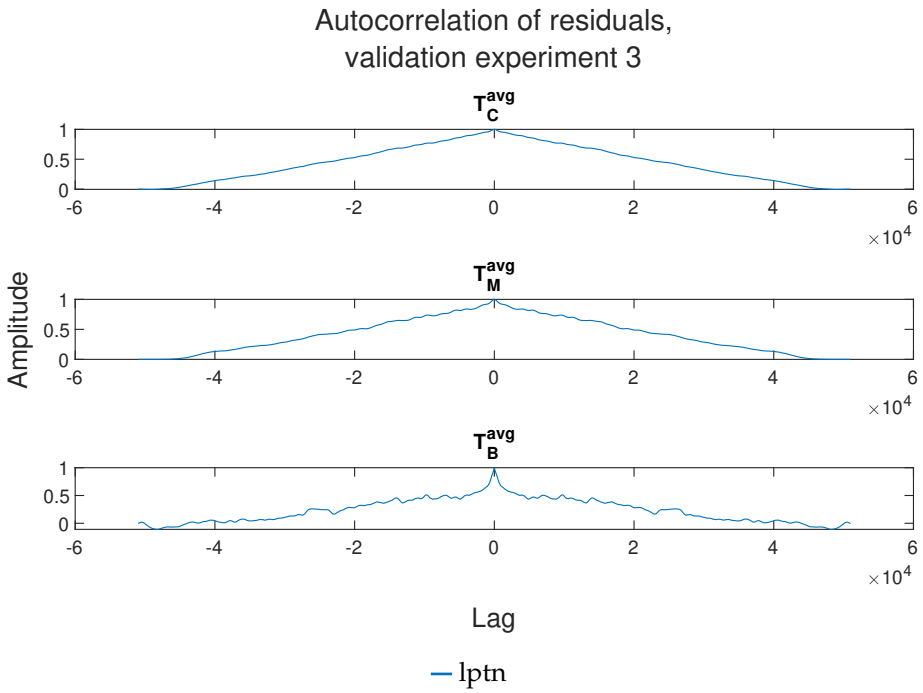

Figure 4.55: The residual autocorrelation of the LPTN for validation experiment 3.

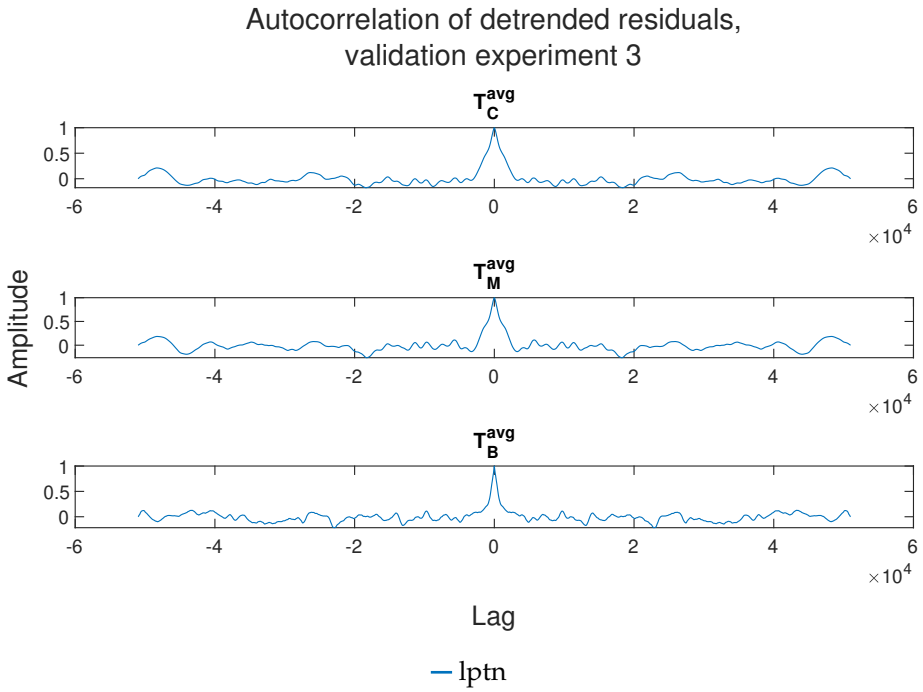

Figure 4.56: The detrended residual autocorrelation of the LPTN for validation experiment 3.

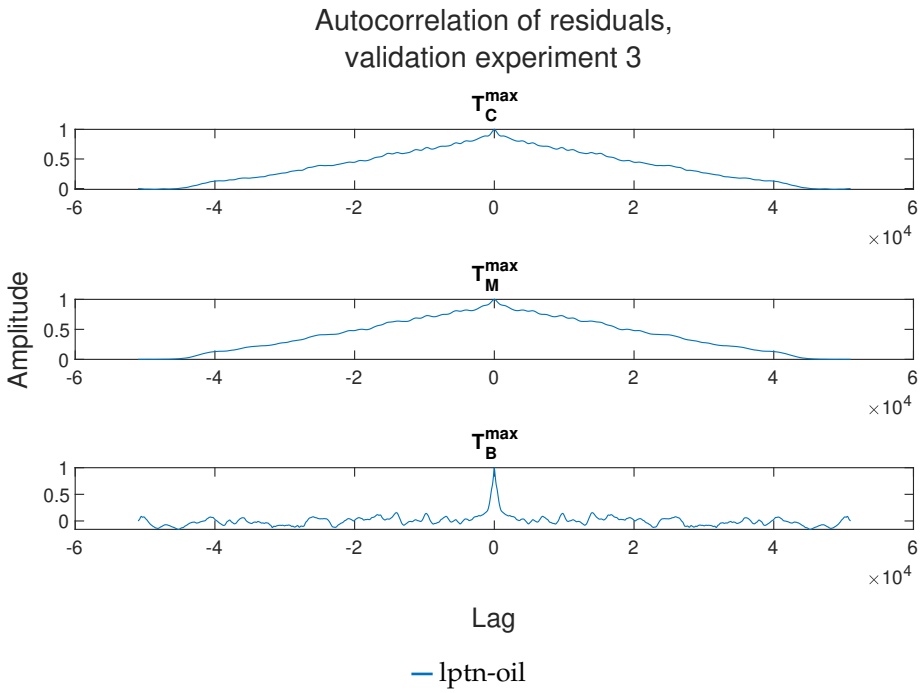

Figure 4.57: The residual autocorrelation of the LPTN-oil models for validation experiment 3.

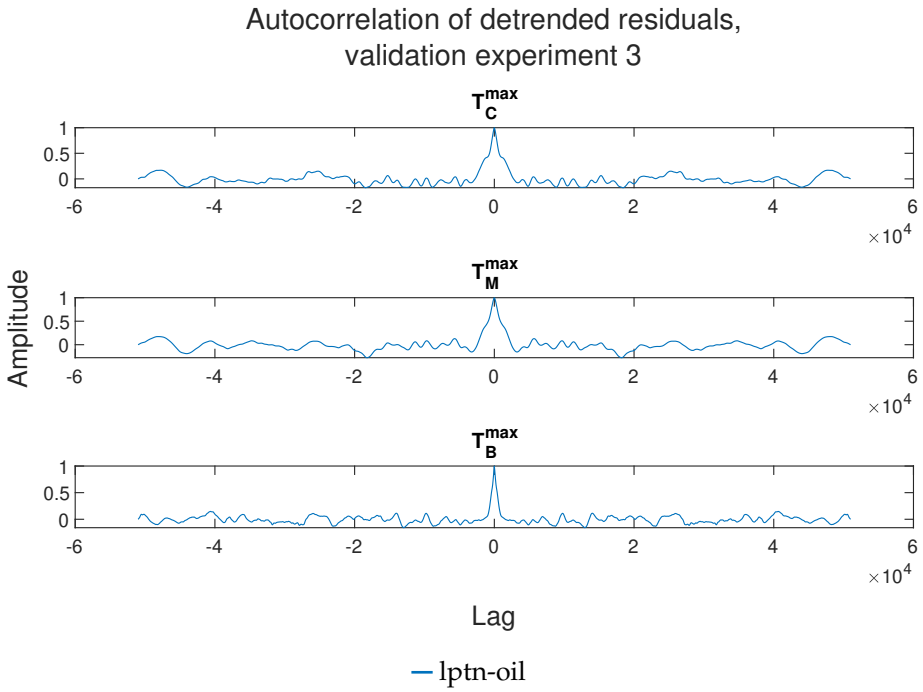

Figure 4.58: The detrended residual autocorrelation of the LPTN-oil models for validation experiment 3.

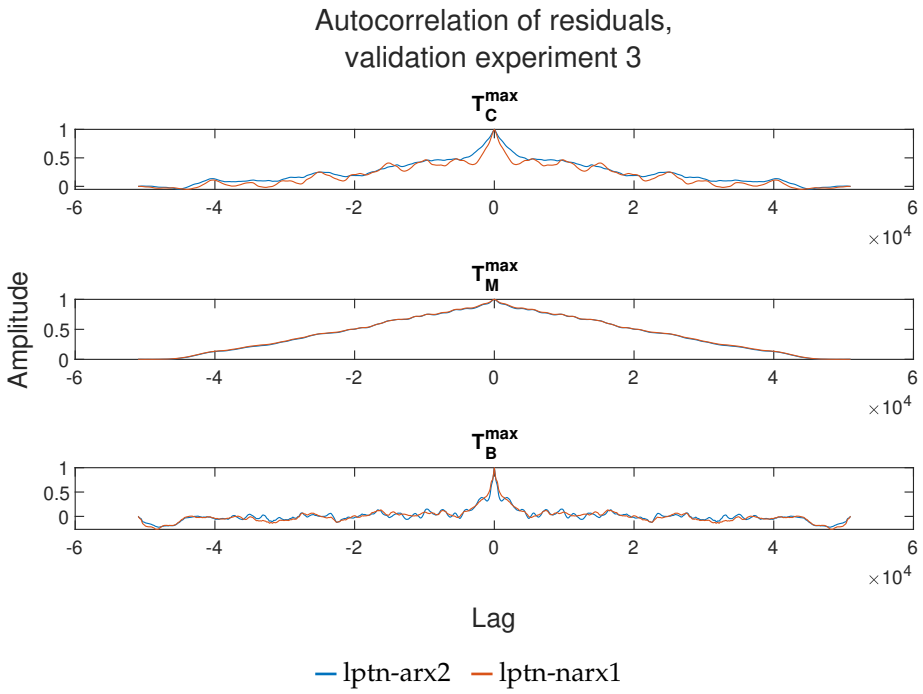

Figure 4.59: The residual autocorrelation of the LPTN-black-box models for validation experiment 3.

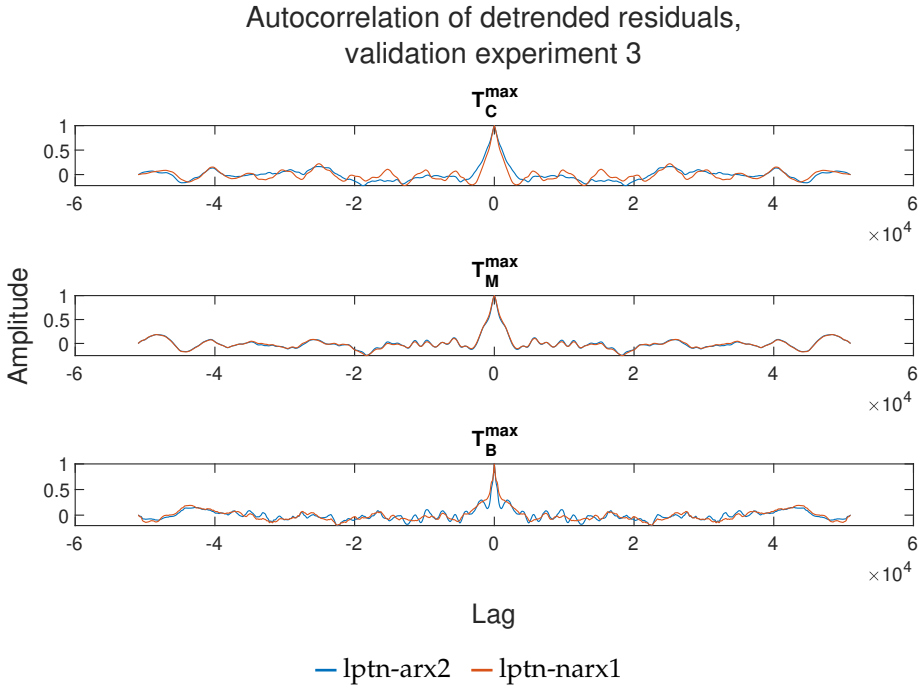

Figure 4.60: The detrended residual autocorrelation of the LPTN-black-box models for validation experiment 3.

Model fit percentages

Table 4.3 compares the fit percentages between the model outputs and the validation experiment. Note that the LPTN is evaluated against the average winding temperatures, and not the maximum as the other models are.

Table 4.3: Model fit percentages of the simulated model outputs for validation experiment 3. Values range between 100 and -∞ where 100 is the best possible fit.

	T_C	T_M	T_B
ARX2	76.72	-1.55	75.05
NARX1	78.36	-3.40	63.77
NARX2	78.29	11.49	74.14
ARX2-Mod	-	8.31	-
NARX1-Mod	-	7.74	-
LPTN	-1.84	-189.18	67.45
LPTN-ARX2	59.11	-152.40	74.63
LPTN-NARX1	62.65	-163.90	76.53
LPTN-Oil	19.41	-223.76	71.79

4.4 Special case

In validation experiment 3, the PMSM suddenly went idle after approximately 5000 seconds. As a consequence, the measured temperatures converged toward the same decreasing values as seen in Figure 4.61 and 4.62. The models' responses to this are depicted in Figure 4.63 - 4.70.

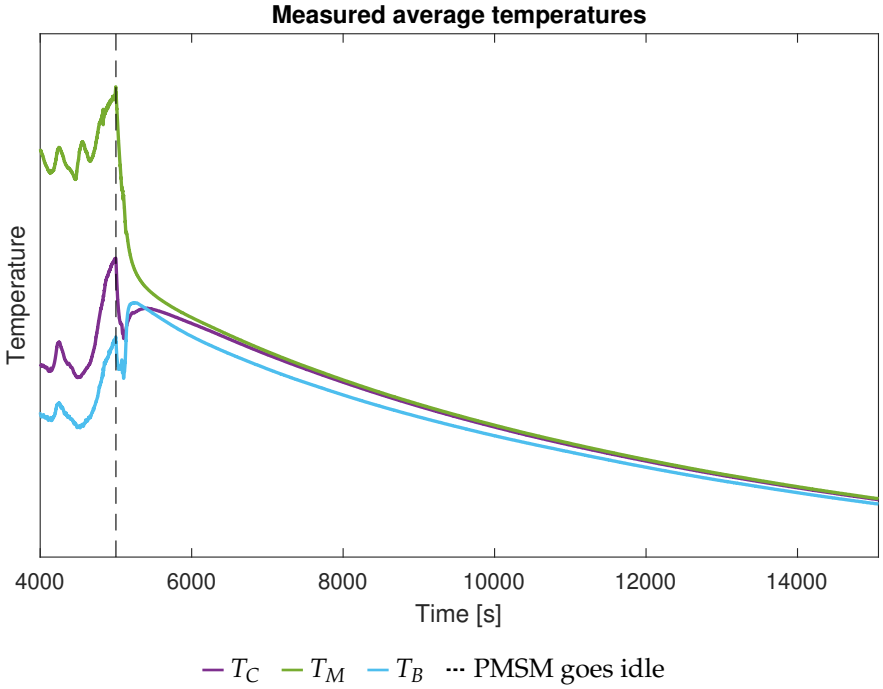

Figure 4.61: The measured average values for the special case.

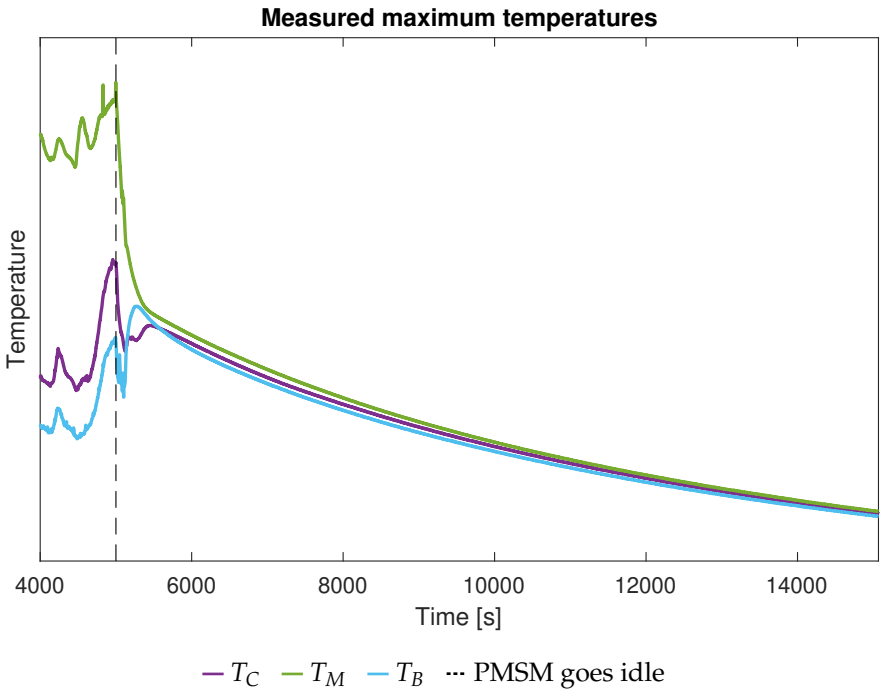

Figure 4.62: The measured maximum values for the special case.

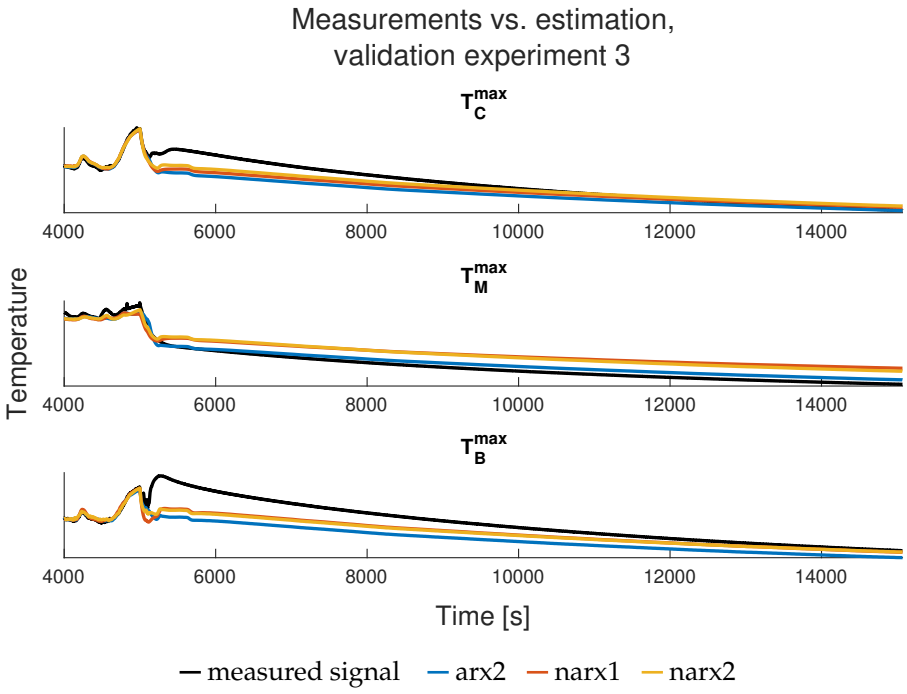

Figure 4.63: Comparison between the temperatures in the special case and the simulated outputs of the black-box models.

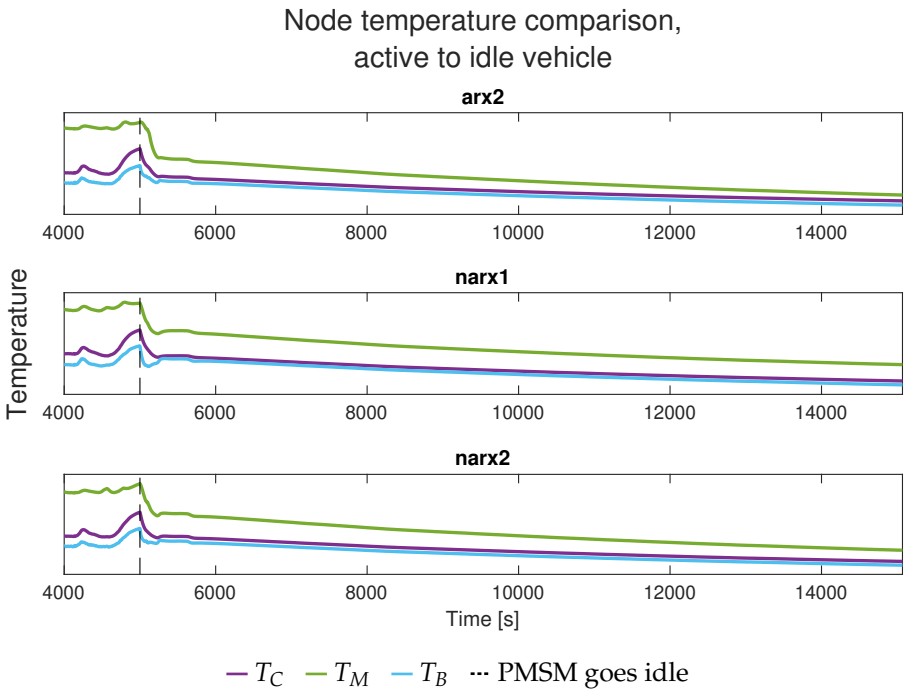

Figure 4.64: Comparison of the node temperatures estimated by the black-box models in the special case.

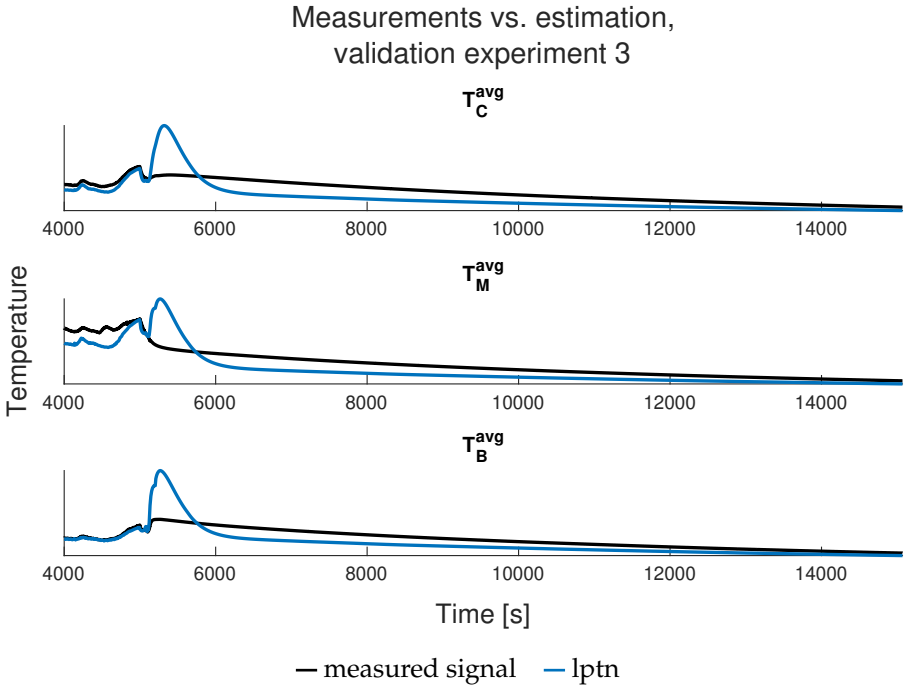

Figure 4.65: Comparison between the temperatures in the special case and the simulated outputs of the LPTN.

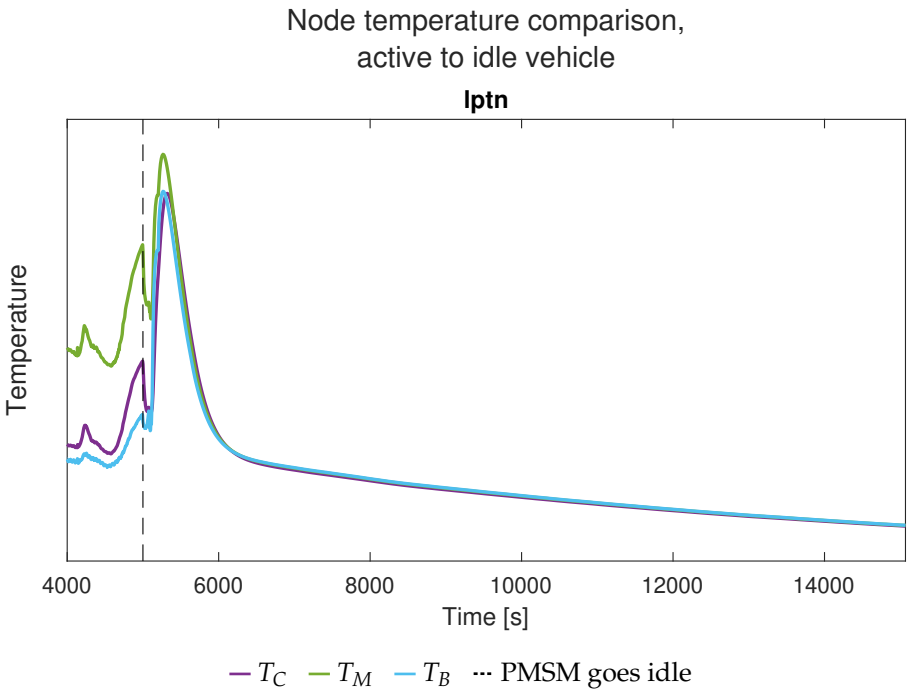

Figure 4.66: Comparison of the node temperatures estimated by the LPTN in the special case.

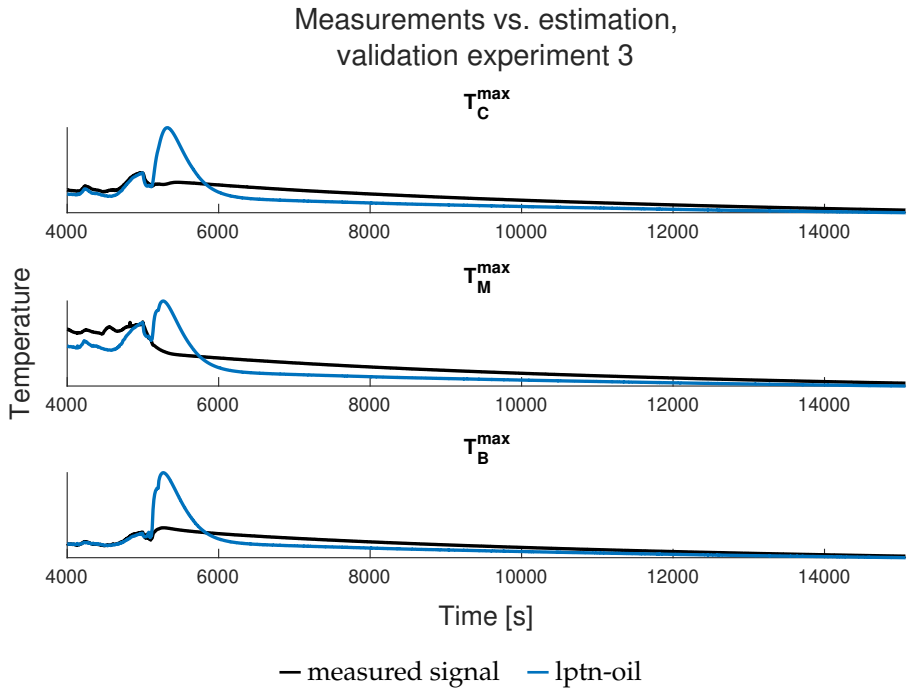

Figure 4.67: Comparison between the temperatures in the special case and the simulated outputs of the LPTN-oil model.

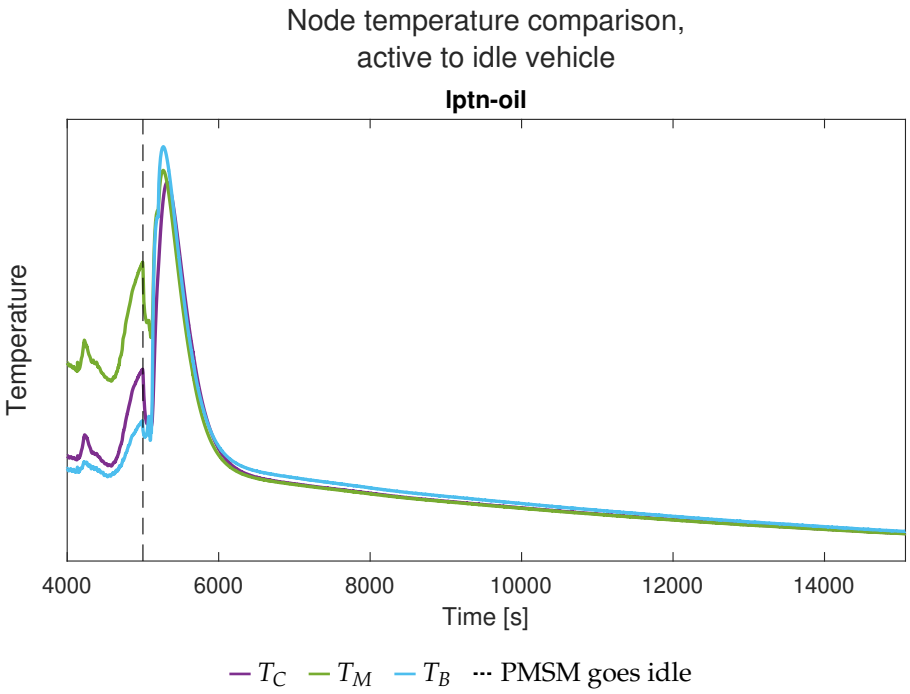

Figure 4.68: Comparison of the node temperatures estimated by the LPTN-oil model in the special case.

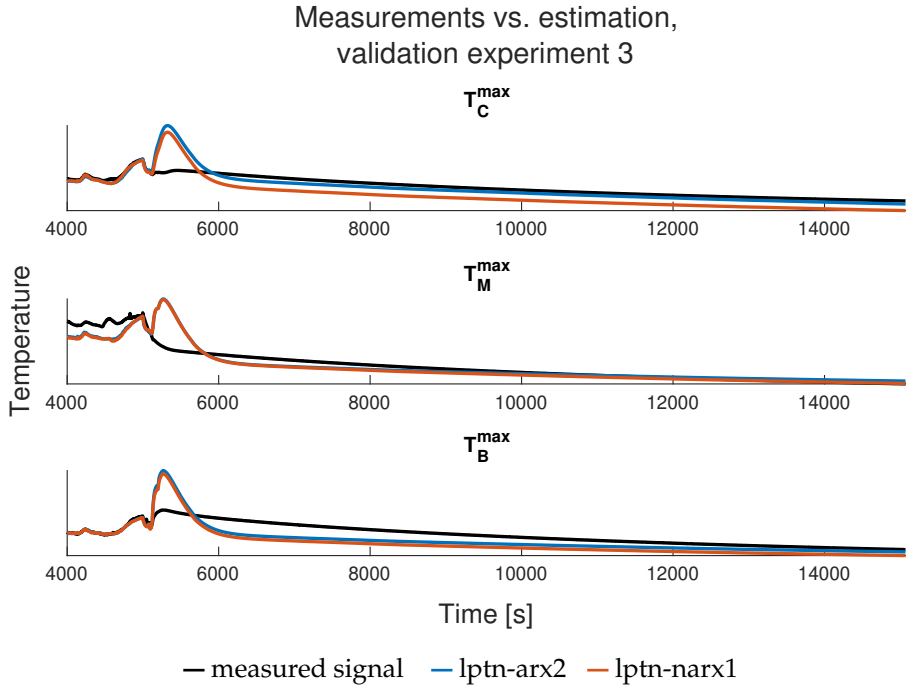

Figure 4.69: Comparison between the temperatures in the special case and the simulated outputs of the LPTN-black-box models.

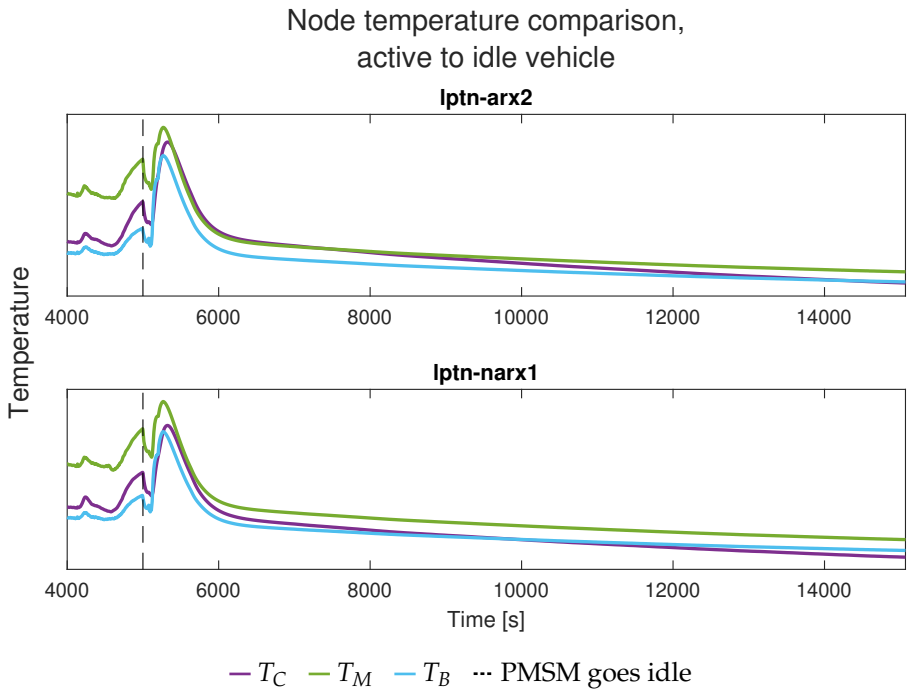

Figure 4.70: Comparison of the node temperatures estimated by the LPTN-black-box models in the special case.

5 Discussion

In this chapter, the results and the methods used for producing them are discussed. Notable results are commented on and attempted to be explained. The methodology is then reviewed before the societal aspects of the thesis are discussed.

5.1 Results

To begin with, the results of the black-box models are discussed. This is followed by discussions of the LPTN-based models, general results, and the special case.

Black-box models

The purely data-driven models are, given that they possess no physical knowledge about the system, surprisingly accurate. Aside from in T_M in Figure 4.41, the residuals stay within the accuracy aim most of the time. In validation experiments 1 and 3, simply removing the constant trends of the residuals results in a white noise-like residual (see Figure 4.12 and 4.52). This means that even if the models are biased, the shapes of some model outputs greatly resemble the shape of the validation data. Thus, adding a constant term could improve the performance.

Using T_C and T_B as inputs for estimating T_M (*arx2-mod* and *narx1-mod*) did not improve the results in any remarkable way. Besides an increase in fit percentage in Table 4.3, the results stayed essentially the same. A reason for this might be that the dynamics of T_C and T_B are too similar to the oil temperature, meaning that very little new information is provided with this method. Even though T_M affects T_C and T_B and vice versa, there is no way for a black-box model to know that. Also, as seen in the LPTN, knowledge of the temperatures of its neighbouring nodes does not equal accurate estimations in M.

No model structures other than ARX and NARX appear in the results. This is due to difficulties producing stable ARMAX models, while OE and BJ models never converged. As mentioned in 2.2, predictors are always stable in ARX models as opposed to in the other linear model structures. It is likely that the system simply is too complex for linear models other than ARX to estimate.

LPTN-based models

While the LPTN-based models perform well in estimating T_B in some cases, and the residual autocorrelations in Figure 4.56 indicate that the model outputs very much resemble the shape of the validation data, they generally perform quite poorly. Even when initialised to the correct temperatures, the LPTN-based models are much slower than the real system in the step experiments. In online applications, initialisation is much more difficult as the real temperatures are unknown. As seen in e.g. Figure 4.5, many minutes can pass before the LPTN reaches the lower bound of the accuracy aim. During this time, the PMSM can reach detrimental temperatures that could be avoided would the cooling system be informed of the high temperatures in time. If the model is initiated when the winding temperature is already high, a good initialisation method is even more important. While not included in the scope of this thesis, initialisation is an interesting and essential subject for not only thermal PMSM models but for the modelling of dynamic systems in general.

As seen in validation experiment 3, the shapes of the measured T_C and T_B are very similar to each other. T_M, on the other hand, looks slightly different. However, the shape of the LPTN model output for T_M looks very much like its estimations of T_C and T_B. This indicates that the node M is too large for the LPTN to thermally model, as the system dynamics change somewhere between the end windings and M.

On a positive note, the residuals of the average temperature estimating LPTN are rather similar to the residuals of the maximum temperature estimating LPTN-oil and LPTN-black-box models. This suggests that the relationship between the average and maximum temperatures has been identified. If the LPTN is improved, the LPTN-based maximum temperature estimating models would, presumably, also improve.

General results

While the produced models estimated T_C and T_B relatively well, they had difficulties finding accurate estimates of T_M. This is a problem since M is the node that reaches the highest temperatures. The reasons behind T_M being both larger and more difficult to model than T_C and T_B are likely the same; C and B are in direct contact with coolant oil, whose temperature is also measured. Naturally, this suggests that they are both cooler, and easier to model. Additionally, the models consider neither the permanent magnets nor the rotor of the PMSM. These are components that contribute to heat in M, but not directly in C or B.

Compared to the results in the literature mentioned in 2.7, the results of this thesis are decent. However, in most papers, validation data did not appear to include drive cycles, nor did the PMSMs reach particularly high temperatures. Furthermore, most papers apply to passenger car EVs, while this thesis concerns heavy-duty EVs. Nonetheless, the LPTN developed in this project was without a doubt expected to perform better.

Regarding residual autocorrelations, note that an improvement by removing the trend of the residual does not necessarily mean that the model is any good. In Figure 4.45, adding a constant term to the model output of T_M would, without a doubt, improve the model fit overall. It would, however, not change the regular over- and undershoots of the model. That would require a more comprehensive change to the model. Furthermore, one has to consider all three validation experiments before adding a term to the output of a model. Improving the model output for one experiment does, of course, not necessarily mean that the model performs better on other data. With that said, the autocorrelation of detrended residuals can highlight the potential of a model, that it has understood the general pattern of the signal

it is trying to estimate. For T_B in Figure 4.31 for instance, *narx2* is clearly the better model. However, Figure 4.32 suggests that *arx2* might model the shape of T_B in a better way.

The special case

As seen in Figure 4.61 and 4.62, the measured temperatures of all nodes converge with each other when the PMSM goes idle. This is expected since no power losses are present, and thus no heat is added to the system. This means that every node will converge with the temperature of its surroundings. In Figure 4.63 - 4.70, it is clear that the node temperatures of the LPTN are dependent on each other while that is not the case for the black-box models. The models have all been calibrated on data from an active PMSM where the power losses, and thus temperatures, are different in each node. For all black-box models, including the LPTN-black-box models, this means that even when the PMSM is idle, the models are going to estimate the temperatures differently. It is not vital that the models can estimate the temperatures accurately when the vehicle is idle since the PMSM is going to cool down anyway. However, this indicates a general understanding of the system which might be valuable for input values outside the scope of the calibration data. In this special case, the input values are much lower than the ones in the calibration experiments. If values are instead much higher, the outputs of the black-box models would likely have to be saturated, while the LPTN might still output reasonable values. This is a large drawback with the black-box models and an advantage of the LPTN.

5.2 Methodology

Many modifications could have been made in the methods used in this thesis. These are discussed more in detail below.

LPTN

The majority of the project's time was spent developing the LPTN as it was believed that physical knowledge of the system would produce the best results. In this thesis, this was not the case, as the purely data-driven models performed better. Regardless, the LPTN definitely showed signs of potential, resembling the general shape of the validation data. The most significant challenge for producing the LPTN was the calibration of the convective parameters $\lambda_{CO}, \lambda_{BO}$, and λ_{SO}. As they were estimated as third-order polynomial functions of the coolant flow, a considerable amount of freedom was given to the model. However, since the coolant flow is not the only non-constant dependency of the convective heat transfer coefficients, calculating them using equations (2.11)-(2.14) could have improved the model as viscosity and thermal conductivity are dependent on temperature. At the very least, the addition of physical properties of the flow and dimensions of the motor would likely not hurt.

As mentioned in 5.1, M was most likely too large. Therefore, adding more nodes at the windings could be another possibility for improving the LPTN. Also, considering the permanent magnets and the rotor of the PMSM could give the model a better understanding of T_M. For these efforts to be possible, though, additional sensors would be needed. They would also increase the computational demands which could impact the feasibility of online estimation.

Black-box models

Considering the relatively little time spent on the black-box models, they were surprisingly accurate. In hindsight, more time could have been spent on them, as many of their aspects were not explored in this thesis. For instance, the time delays, n_k, were set to 0 for each

input-output pair in the black-box models. This was mostly due to time constraints, as estimating them would take valuable time from other elements of the thesis. It would, however, be interesting to investigate how more suitable values of n_k would affect the performance as T_M is not immediately affected by the oil temperature for instance. Exploring different regressors of the NARX model and different non-linearities in Hammerstein-Wiener models would also be interesting.

As (2.9) suggested model orders from 3 to 6, and the best-performing black-box models were of orders 1 and 2, it was clearly not a suitable method for model order selection in this case. This can be explained by the fact that the method applies to linear systems, while the system in question was non-linear. Furthermore, the method assumes that measurement noise is not present in the data. If the filtering of the data was perfect, this would be true. However, there is of course a possibility that the data could have been filtered in a better way. Luckily, the model order selection method was solely used to get a hint of which orders to start with and did not affect the results since more orders than what was suggested were tried.

Model calibration

Due to the importance of accuracy at high temperatures, it would be reasonable for the models to be calibrated using cost functions based on the temperature. In this thesis, the models were calibrated in a way that does not punish inaccuracy at high temperatures particularly. Instead, accuracy was just as valuable at low temperatures as it was at high temperatures. This could improve the performance of all models in cases where accuracy really matters.

Since all models need data for calibration, new hardware versions mean that the models need to be re-calibrated. A model purely based on physical relationships would eliminate this need, as only dimensions and physical properties would have to be updated. However, these types of models are rarely accurate unless they are very complex and demand heavy computations.

Model validation

Additional and different model validation methods could have been used. Many are mentioned in [15]; modelling the residuals, analysing cross-correlations between residuals and previous inputs, and comparing the frequency functions of the model to the ones of the system to name a few. Would the models be calibrated to prioritise accuracy at high temperatures, (2.10) could be modified accordingly.

5.3 The work in a wider context

The main motivation for this thesis was to extend the life of PMSMs and, consequently also EVs. As the electrification of the automotive industry is an essential part of fighting climate change, this is a highly important subject. However, the methods used in this thesis require plenty of data, which in turn requires a lot of energy to collect. If a good model can be produced from this, it can save energy in the long run. However, there is no way of instantly knowing if the model is accurate during real driving. A model might be underestimating the temperature and the PMSM will be damaged anyway. Also, performance degradation from exposing a PMSM to harmful temperatures might not be apparent immediately. Thus, it can take years before the usefulness and accuracy of a thermal model is known. Furthermore, cooling and torque limiting strategies based on other aspects than temperature could be more effective. It might be enough to develop a strategy based on the torque alone. Nevertheless,

a good thermal model can contribute to extending the life of PMSMs and thus also have a positive effect on the environment.

6 Conclusion

In this master's thesis, the hot spot temperatures of PMSM windings were modelled using different methods. Several black-box models were calibrated, and a lumped parameter thermal network was designed and combined with black-box models and a simple oil temperature-based model. The results show that none of the models was sufficient for achieving the desired accuracy goals, even if the black-box models were quite close. This was despite lacking physical knowledge of the system, which also meant that the least amount of time was needed to implement them since no physical relations needed to be derived.

Looking back at the research questions, the results show that they can be answered in the following way:

- **How do common black-box models for estimating the hot spot temperature of PMSM windings perform?**
  Out of the black-box models investigated in this master's thesis, ARX and NARX were the best performing, estimating the temperatures of the end windings well. The mid-stack winding temperature, however, was more challenging to model. The system was assumed too complex for ARMAX, OE, and BJ models to be produced.

- **How can physical knowledge of a PMSM be incorporated in the construction of a model that fulfils the desired accuracy?**
  While the desired accuracy was not fulfilled, physical knowledge was incorporated into an LPTN which showed clear signs of system understanding. To improve the model further, more information regarding the coolant flow could be added, as well as more nodes.

In conclusion, black-box models are to be preferred out of the models investigated in this thesis, considering both implementation complexity and performance. A more detailed LPTN might have the potential to be more accurate but takes more time to implement. More parts of the PMSM might need to be considered to fulfil the desired accuracy. This includes both more parts of the windings and more components, such as the permanent magnets and the rotor.

Bibliography

[1] Nic Lutsey. "Global climate change mitigation potential from a transition to electric vehicles". In: *The International Council on Clean Transportation* 5 (2015).

[2] Emmanuel Agamloh, Annette Von Jouanne, and Alexandre Yokochi. "An overview of electric machine trends in modern electric vehicles". In: *Machines* 8.2 (2020), p. 20.

[3] David Dorrell, Leila Parsa, and Ion Boldea. "Automotive Electric Motors, Generators, and Actuator Drive Systems With Reduced or No Permanent Magnets and Innovative Design Concepts". In: *IEEE Transactions on Industrial Electronics* 61.10 (2014), pp. 5693–5695. DOI: 10.1109/TIE.2014.2307839.

[4] Shigeo Morimoto, Yoshinari Asano, Takashi Kosaka, and Yuji Enomoto. "Recent technical trends in PMSM". In: *2014 International Power Electronics Conference (IPEC-Hiroshima 2014 - ECCE ASIA)*. 2014, pp. 1997–2003. DOI: 10.1109/IPEC.2014.6869862.

[5] Silong Li, Bulent Sarlioglu, Sinisa Jurkovic, Nitin R. Patel, and Peter Savagian. "Analysis of Temperature Effects on Performance of Interior Permanent Magnet Machines for High Variable Temperature Applications". In: *IEEE Transactions on Industry Applications* 53.5 (2017), pp. 4923–4933. DOI: 10.1109/TIA.2017.2700473.

[6] Ayman M El-Refaie. "Motors/generators for traction/propulsion applications: A review". In: *IEEE Vehicular Technology Magazine* 8.1 (2013), pp. 90–99.

[7] Zureks. *Stator and rotor of a three-phase induction motor: 0.75 kW, 1420 rpm, 50 Hz, 230-400 V AC, 3.4-2.0 A*. https://commons.wikimedia.org/wiki/File:Stator_and_rotor_by_Zureks.JPG. This work is licensed under the Creative Commons Attribution-Share Alike 3.0 Unported licence. To view a copy of this licence, visit https://creativecommons.org/licenses/by-sa/3.0/deed.en. 2008.

[8] Christian Kral, Anton Haumer, and Sang Bin Lee. "A practical thermal model for the estimation of permanent magnet and stator winding temperatures". In: *IEEE Transactions on Power Electronics* 29.1 (2013), pp. 455–464.

[9] Ahmed Selema, Mohamed N Ibrahim, and Peter Sergeant. "Electrical machines winding technology: Latest advancements for transportation Electrification". In: *Machines* 10.7 (2022), p. 563.

[10] Maki K. Habib, Samuel A. Ayankoso, and Fusaomi Nagata. "Data-Driven Modeling: Concept, Techniques, Challenges and a Case Study". In: *2021 IEEE International Conference on Mechatronics and Automation (ICMA)*. 2021, pp. 1000–1007. DOI: 10.1109/ICMA52036.2021.9512658.

[11] Urban Forssell and Lennart Ljung. "Identification of unstable systems using output error and Box-Jenkins model structures". In: *IEEE Transactions on Automatic Control* 45.1 (2000), pp. 137–141.

[12] Edwin Reynders. "System identification methods for (operational) modal analysis: review and comparison". In: *Archives of Computational Methods in Engineering* 19 (2012), pp. 51–124.

[13] Gaetan Kerschen, Keith Worden, Alexander F Vakakis, and Jean-Claude Golinval. "Past, present and future of nonlinear system identification in structural dynamics". In: *Mechanical systems and signal processing* 20.3 (2006), pp. 505–592.

[14] Adrian Wills, Thomas B Schön, Lennart Ljung, and Brett Ninness. "Identification of hammerstein–wiener models". In: *Automatica* 49.1 (2013), pp. 70–81.

[15] Lennart Ljung. *System Identification: Theory for the User*. Address of the Publisher: Pearson Education, 1999.

[16] Mathworks. *Compare identified model output with measured output*. https://se.mathworks.com/help/ident/ref/compare.html. Accessed: 2023-05-17.

[17] Anthony F Mills. *Heat transfer*. CRC Press, 1992.

[18] M Necati Ã–zisik and M Necati Özışık. *Heat conduction*. John Wiley & Sons, 1993.

[19] Latif M Jiji and Latif Menashi Jiji. *Heat convection*. Springer, 2006.

[20] Robert Siegel. *Thermal radiation heat transfer*. CRC press, 2001.

[21] R Shankar Subramanian. "Heat transfer in flow through conduits". In: *Department of Chemical and Biomolecular Engineering, Clarkson University Project* (2015).

[22] Y Cengel and Transfer Mass Heat. "A practical approach". In: *Heat and Mass Transfer* (2003).

[23] Anthony F Mills. *Heat transfer*. CRC Press, 1992.

[24] Malcolm W Chase and National Information Standards Organization (US). *NIST-JANAF thermochemical tables*. Vol. 9. American Chemical Society Washington, DC, 1998.

[25] Carl Nordling and Jonny Österman. *Physics Handbook for Science and Engineering*. 8:5. Studentlitteratur AB, Jan. 2006.

[26] Jörg Schützhold and Wilfried Hofmann. "Analysis of the temperature dependence of losses in electrical machines". In: *2013 IEEE Energy Conversion Congress and Exposition*. IEEE. 2013, pp. 3159–3165.

[27] John M Eargle and John M Eargle. "Resistance Change with Temperature for Copper". In: *Electroacoustical Reference Data* (2002), pp. 106–107.

[28] Sina Khalesidoost, Jawad Faiz, and Ehsan Mazaheri-Tehrani. "An overview of thermal modelling techniques for permanent magnet machines". In: *IET Science, Measurement & Technology* 16.4 (2022), pp. 219–241.

[29] Daesuk Joo, Ju-Hee Cho, Kyungil Woo, Byung-Taek Kim, and Dae-Kyong Kim. "Electromagnetic Field and Thermal Linked Analysis of Interior Permanent-Magnet Synchronous Motor for Agricultural Electric Vehicle". In: *IEEE Transactions on Magnetics* 47.10 (2011), pp. 4242–4245. DOI: 10.1109/TMAG.2011.2149504.

[30] Dawei Liang, ZQ Zhu, Yafeng Zhang, Jianghua Feng, Shuying Guo, Yifeng Li, Jiangquan Wu, and Anfeng Zhao. "A hybrid lumped-parameter and two-dimensional analytical thermal model for electrical machines". In: *IEEE Transactions on Industry Applications* 57.1 (2020), pp. 246–258.

[31] Tianfu Sun, Jiabin Wang, Antonio Griffo, and Bhaskar Sen. "Active thermal management for interior permanent magnet synchronous machine (IPMSM) drives based on model predictive control". In: *IEEE Transactions on Industry Applications* 54.5 (2018), pp. 4506–4514.

[32] Oludare Isaac Abiodun, Aman Jantan, Abiodun Esther Omolara, Kemi Victoria Dada, Nachaat AbdElatif Mohamed, and Humaira Arshad. "State-of-the-art in artificial neural network applications: A survey". In: *Heliyon* 4.11 (2018), e00938.

[33] Jun Lee and Jung-Ik Ha. "Temperature estimation of PMSM using a difference-estimating feedforward neural network". In: *IEEE Access* 8 (2020), pp. 130855–130865.

[34] Emebet Gebeyehu Gedlu, Oliver Wallscheid, and Joachim Böcker. "Temperature estimation of electric machines using a hybrid model of feed-forward neural and low-order lumped-parameter thermal networks". In: *2021 IEEE International Electric Machines Drives Conference (IEMDC)*. 2021, pp. 1–8. DOI: 10.1109/IEMDC47953.2021.9449548.